Cosmic voids from a spacetime-dependent scale factor $R(t, x, y, z)$: exact Einstein equations, negative-curvature domains, and confrontation with galaxy statistics

Moninder Singh Modgil[1, *]

[1] *SpARC, Gyansarovar, Mount Abu, Rajasthan, India*

(Dated: November 2, 2026)

We generalize the Friedmann–Lemaître–Robertson–Walker (FLRW) line element by promoting the scale factor to a function of space and time, $ds^2 = -c^2dt^2 + R^2(t, \mathbf{x})\,\delta_{ij}dx^i dx^j/(1+kr^2/4)^2$, and ask whether such a geometry can account for the large voids observed in the galaxy distribution. Writing $R/(1 + kr^2/4) \equiv e^{\alpha(t,\mathbf{x})}$, we derive the complete Einstein tensor without approximation and decompose it, relative to the comoving observers $u^a = \delta^a_0$, into an energy density, an isotropic pressure, an energy flux and an anisotropic stress. The comoving congruence is geodesic, shear-free and irrotational; its Weyl tensor is purely electric and equal to $4\pi G$ times the anisotropic stress. We prove that the source is a perfect fluid only if the metric is FLRW, so that any void requires an imperfect effective fluid. The Hamiltonian constraint becomes a Lichnerowicz equation for $e^{\alpha/2}$, which allows any observed void density profile to be reconstructed exactly as a domain of negative spatial curvature; for a void of radius $30\,h^{-1}\,$Mpc and central contrast -0.85 the conformal factor is depressed by only 4.8×10^{-6}, while the local curvature parameter reaches $\Omega_k^{\rm loc} = 0.27$. We study three closures. A static spatial factor makes the inhomogeneity behave as a $w = -1/3$ "curvature fluid" whose contrast grows as a at all times; a pressureless closure gives acoustic oscillations with $c_s = c/\sqrt{3}$; and a growth-matched closure reproduces ΛCDM growth by construction. In all cases the absence of a lapse perturbation halves gravitational lensing relative to general relativity at fixed density, giving $E_G = \Omega_m/(2f)$. We complement the theory with a statistical analysis of 3×10^5-galaxy mock catalogues in a $(1\,h^{-3}\,{\rm Gpc}^3)$ volume: power spectra, Landy–Szalay correlation functions, counts-in-cells moments, void probability functions, genus statistics and some 3 500 voids per catalogue. We find that 95% of void centres lie in regions of negative smoothed spatial curvature, and that the static-factor model is distinguished from ΛCDM by its void size function at $z = 0$ with Kolmogorov–Smirnov $p \sim 10^{-86}$. An exact Lemaître–Tolman–Bondi void evolved from the same initial profile shows that the static model is valid only while $|\delta| \ll 1$: for a linear contrast of -2 the exact central contrast is -0.72, and the LTB void expands 30% faster than the background. Redshift-space power-spectrum and void–galaxy quadrupoles of the mocks vanish for the static model and change sign for the growth-matched one. A fit to eight $f\sigma_8$ and five E_G measurements disfavors the two closures by $\Delta\chi^2 = 72$ and 21 relative to ΛCDM. Restoring a spatially varying lapse, $ds^2 = -N^2dt^2 + R^2d\mathbf{x}^2$, admits perfect fluids, recovers ΛCDM dynamics with no gravitational slip, and keeps the Lichnerowicz description of voids. The spatially varying scale factor is thus the correct description of the spatial geometry of voids, while their dynamics requires the lapse.

I. INTRODUCTION

The galaxy distribution on scales of tens of megaparsecs is dominated by underdense regions. The first redshift surveys found large empty regions in front of the Coma cluster [1] and the Boötes void, of order 100 Mpc across [2, 3]. Wide-angle surveys then revealed a "slice of the universe" in which galaxies lie on the walls of bubble-like voids [4, 5]. This picture was confirmed by the 2dFGRS [6] and SDSS [7], by the Sloan Great Wall [8] and by systematic void catalogues [9–14]. Voids are now a cosmological probe in their own right, through their abundance, shapes, density profiles and the dynamics of galaxies around them [15–20]. A few unusually large or deep underdense regions, such as the local KBC void [21] and the Eridanus supervoid aligned with the CMB Cold Spot [22], are at the edge of what is expected in the standard model; whether the abundance and emptiness of voids is fully understood has been debated [23, 24].

In the standard ΛCDM model voids are the counterparts of collapsed structures: underdense regions of the initial Gaussian field expand faster than the background, evacuate, and form a hierarchy of merging and collapsing voids [25–31]. The background is the homogeneous and isotropic FLRW metric [32–35], and structure is described by perturbations around it [36–40]. Exact inhomogeneous solutions offer a complementary route. The Lemaître–Tolman–Bondi (LTB) models [41–43], the Szekeres family [44] and the Stephani models [45] have been used to describe voids and to test the Copernican principle [46–49]; averaging and backreaction have been studied in the same context [50, 51].

The idea of a scale factor that varies across space has a long history. Lemaître's 1933 solution already assigns each spherical shell its own scale factor [41]. The "separate universe" picture of long-wavelength perturbations treats each region as an FLRW model with its own curvature, and is the basis of the spherical-collapse

* msmodgil@gmail.com

and spherical-void models [28, 30]. Gradient expansions of the Einstein equations make this idea systematic on super-horizon scales. In the conformal method of the initial-value problem, a conformally flat spatial metric $\phi^4\delta_{ij}$ is the standard ansatz [65, 66]. What has not, to our knowledge, been worked out in detail is the opposite and simplest route: to take the FLRW form literally with $R = R(t, \mathbf{x})$, derive what it implies exactly, and confront it with the statistics of voids. That is the purpose of this paper.

In this paper we study perhaps the simplest generalization of FLRW: keep the lapse equal to one and the spatial metric conformally flat, but let the scale factor depend on position,

$$ds^2 = -c^2dt^2 + \frac{R^2(t,x,y,z)}{\left(1+\frac{1}{4}kr^2\right)^2}\left(dx^2+dy^2+dz^2\right), \quad (1)$$

Equation (1) reduces to FLRW when $R = a(t)$. with $r^2 = x^2 + y^2 + z^2$. It is an appealing phenomenological model of voids: a region in which R is larger, or in which the spatial geometry is locally more open, should contain fewer galaxies. Our aims are:

1. to derive the Einstein equations for Eq. (1) exactly, together with the kinematics of the comoving observers, the Weyl curvature, the conservation laws and the energy conditions;
2. to determine what matter content the geometry requires, and whether it can be a perfect fluid;
3. to construct voids explicitly, and to compute their lensing and integrated Sachs–Wolfe (ISW) signatures;
4. to compare the model with the statistics of the galaxy distribution, using mock catalogues analyzed with standard estimators, in real and redshift space;
5. to compare its void evolution with an exact Lemaître–Tolman–Bondi void;
6. to fit it to published growth-rate and lensing data;
7. to identify the minimal extension, a spatially varying lapse, that cures its difficulties.

Our main results are as follows. (i) The Einstein tensor is given in closed form [Eqs. (13)–(15)]; the comoving observers are geodesic, shear-free and irrotational, and the electric Weyl tensor equals $4\pi G$ times the anisotropic stress [Eq. (33)]. (ii) The source is a perfect fluid only for FLRW (Theorem 1), so voids require an effective imperfect fluid. (iii) The Hamiltonian constraint is a Lichnerowicz equation [Eq. (70)], so any void profile can be reconstructed exactly. Voids are domains of negative spatial curvature, and their conformal factor is depressed by a few parts in 10^6. (iv) Three closures give a growth law $D \propto a$, sound waves with $c_s = c/\sqrt{3}$, or ΛCDM growth. (v) Because the lapse is unperturbed, light deflection is half its general-relativistic value at fixed density, and the static model has no redshift-space distortion. (vi) In mock catalogues, 95% of void centres lie in negative-curvature regions; the static model changes the void abundance at $z = 0$ at very high significance. (vii) An exact LTB void shows that the static model is a linear approximation that fails for $|\delta| \gtrsim 0.3$ and misses the faster expansion of voids. (viii) Redshift-space quadrupoles vanish (static) or change sign (growth-matched), and a fit to $f\sigma_8$ and E_G data disfavors the two closures by $\Delta\chi^2 = 72$ and 21. (ix) Restoring the lapse, $g_{00} = -e^{2\nu}$, permits perfect fluids and recovers ΛCDM dynamics while keeping voids as negative-curvature domains of R.

The paper is organized as follows. Section II derives the curvature. Section III gives the $1+3$ covariant description and the FLRW theorem. Section IV treats redshift, distances and lensing. Section V relates the model to cosmological perturbation theory and introduces the closures. Section VI constructs voids, Sec. VII compares them with an exact LTB void, Sec. VIII restores the lapse, and Sec. IX discusses local expansion rates and averaging. Section X presents the statistical analysis of the galaxy distribution in real and redshift space, and Sec. XI confronts the model with growth and lensing data. Section XII discusses the results and Sec. XIII concludes. Appendices collect the connection and curvature components, the spherical reduction, the numerical methods, the two-function metric in detail, robustness tests of the void statistics, FLRW-limit consistency checks, series solutions of the Lichnerowicz equation, analytic lensing of a top-hat void and statistical conventions; Appendix A lists the notation. We use signature $(-,+,+,+)$, Latin indices $i, j, \ldots$ for space, and units $c = 1$ in Secs. II–IV unless stated; c is restored for numerical work.

II. GEOMETRY OF A SPACETIME-DEPENDENT SCALE FACTOR

A. Line element and the conformal exponent

Because the curvature factor $(1 + kr^2/4)^{-2}$ in Eq. (1) is itself a function of position, it can be absorbed into the scale factor. We define the *conformal exponent*

$$\alpha(t, \mathbf{x}) \equiv \ln R(t, \mathbf{x}) - \ln\left(1 + \tfrac{1}{4}kr^2\right), \quad (2)$$

so that the metric becomes

$$ds^2 = -dt^2 + e^{2\alpha(t,\mathbf{x})}\delta_{ij}\,dx^i dx^j, \quad (3)$$

i.e. $g_{00} = -1$, $g_{0i} = 0$, $g_{ij} = e^{2\alpha}\delta_{ij}$. All results below are written in terms of α. The FLRW case is

$$\alpha_{\rm FLRW} = \ln a(t) - \ln\left(1 + \tfrac{1}{4}kr^2\right), \quad (4)$$

and the cosmologically relevant decomposition is

$$\alpha(t, \mathbf{x}) = \ln a(t) + \psi(t, \mathbf{x}), \quad R = a(t)\, e^{\psi(t,\mathbf{x})}, \quad (5)$$

for $k = 0$, where $a(t)$ is a background scale factor and ψ measures the local excess of the scale factor. We write $\dot{} \equiv \partial_t$, $\partial_i \equiv \partial/\partial x^i$, $\nabla^2 \equiv \delta^{ij}\partial_i\partial_j$ and $(\nabla\alpha)^2 \equiv \delta^{ij}\partial_i\alpha\,\partial_j\alpha$; these are flat-space operators in the comoving coordinates.

B. Connection

The nonvanishing Christoffel symbols of Eq. (3) are

$$\Gamma^0_{ij} = \dot\alpha\, e^{2\alpha}\delta_{ij}, \tag{6}$$
$$\Gamma^i_{0j} = \dot\alpha\,\delta^i_j, \tag{7}$$
$$\Gamma^i_{jk} = \delta^i_j\,\partial_k\alpha + \delta^i_k\,\partial_j\alpha - \delta_{jk}\,\partial_i\alpha. \tag{8}$$

In particular $\Gamma^0_{00} = \Gamma^0_{0i} = \Gamma^i_{00} = 0$, so the worldlines $x^i = \text{const}$ are geodesics.

C. Ricci and Einstein tensors

The Ricci tensor follows from Eqs. (6)–(8) (details in Appendix B):

$$R_{00} = -3\left(\ddot\alpha + \dot\alpha^2\right), \tag{9}$$
$$R_{0i} = -2\,\partial_i\dot\alpha, \tag{10}$$
$$R_{ij} = e^{2\alpha}\left(\ddot\alpha + 3\dot\alpha^2\right)\delta_{ij} - \partial_i\partial_j\alpha + \partial_i\alpha\,\partial_j\alpha - \delta_{ij}\left[\nabla^2\alpha + (\nabla\alpha)^2\right]. \tag{11}$$

The Ricci scalar is

$$R = 6\left(\ddot\alpha + 2\dot\alpha^2\right) - e^{-2\alpha}\left[4\nabla^2\alpha + 2(\nabla\alpha)^2\right]. \tag{12}$$

The mixed components of the Einstein tensor $G^a{}_b = R^a{}_b - \frac{1}{2}\delta^a_b R$ are

$$G^0{}_0 = -3\dot\alpha^2 + e^{-2\alpha}\left[2\nabla^2\alpha + (\nabla\alpha)^2\right], \tag{13}$$
$$G_{0i} = -2\,\partial_i\dot\alpha, \tag{14}$$
$$G^i{}_j = -\left(2\ddot\alpha + 3\dot\alpha^2\right)\delta^i_j + e^{-2\alpha}\left[\partial_i\alpha\,\partial_j\alpha - \partial_i\partial_j\alpha + \delta_{ij}\nabla^2\alpha\right]. \tag{15}$$

Equations (9)–(15) are exact. We verified them with an independent symbolic computation of the full Riemann tensor for arbitrary $\alpha(t, x, y, z)$. Their structure is transparent: time derivatives enter only through the local Hubble rate $\dot\alpha$, spatial derivatives only through the curvature of the conformally flat three-metric, and the two are coupled only in G_{0i}.

D. Spatial curvature

The hypersurfaces $t = \text{const}$ have induced metric $h_{ij} = e^{2\alpha}\delta_{ij}$, whose Ricci tensor and scalar are

$${}^{(3)}R_{ij} = -\left(\partial_i\partial_j\alpha - \partial_i\alpha\,\partial_j\alpha\right) - \delta_{ij}\left(\nabla^2\alpha + (\nabla\alpha)^2\right), \tag{16}$$
$${}^{(3)}R = -e^{-2\alpha}\left[4\nabla^2\alpha + 2(\nabla\alpha)^2\right] = -8\,e^{-5\alpha/2}\,\nabla^2 e^{\alpha/2}. \tag{17}$$

The last form follows from the identity

$$2\nabla^2\alpha + (\nabla\alpha)^2 = 4\,e^{-\alpha/2}\,\nabla^2 e^{\alpha/2}, \tag{18}$$

and is the origin of the Lichnerowicz form of the constraint (Sec. VI A). For FLRW, Eq. (4) gives ${}^{(3)}R = 6k/a^2$, as it should. We define the local curvature parameter, measured against the background Hubble rate H,

$$\Omega_k^{\rm loc}(t, \mathbf{x}) \equiv -\frac{{}^{(3)}R\,c^2}{6H^2}. \tag{19}$$

A region with $\Omega_k^{\rm loc} > 0$ is locally open.

III. COVARIANT 1+3 DESCRIPTION AND THE MATTER CONTENT

A. Kinematics of the comoving observers

Let $u^a = \delta^a_0$ be the four-velocity of the observers at fixed x^i; then $u_a = -\delta^0_a$ and $h_{ab} = g_{ab} + u_a u_b$ projects onto their rest spaces. The covariant derivative decomposes as [52–55]

$$\nabla_b u_a = -u_b A_a + \tfrac{1}{3}\theta h_{ab} + \sigma_{ab} + \omega_{ab}. \tag{20}$$

With Eqs. (6)–(7) we find $\nabla_j u_i = \Gamma^0_{ij} = \dot\alpha\, h_{ij}$ and $\nabla_0 u_a = 0$. Hence

$$A_a = 0, \qquad \theta = 3\dot\alpha, \qquad \sigma_{ab} = 0, \qquad \omega_{ab} = 0. \tag{21}$$

The comoving congruence is geodesic, expanding, shear-free and irrotational. The local Hubble rate and deceleration parameter are

$$\mathcal{H}(t, \mathbf{x}) \equiv \tfrac{1}{3}\theta = \dot\alpha, \qquad q_{\rm loc}(t, \mathbf{x}) \equiv -1 - \frac{\ddot\alpha}{\dot\alpha^2}. \tag{22}$$

For the decomposition (5), $\mathcal{H} = H + \dot\psi$: a spatially varying scale factor produces a spatially varying expansion rate only if ψ depends on time.

B. Energy–momentum decomposition

Relative to u^a, any energy–momentum tensor can be written as

$$T_{ab} = \rho\, u_a u_b + p\, h_{ab} + q_a u_b + q_b u_a + \pi_{ab}, \tag{23}$$

with $q_a u^a = 0$, $\pi_{ab}u^b = 0$, $\pi^a{}_a = 0$ and $\pi_{ab} = \pi_{\langle ab\rangle}$. Einstein's equations $G_{ab} + \Lambda g_{ab} = 8\pi G\, T_{ab}$, with Eqs. (13)–(15), then give

$$\begin{aligned} 8\pi G\rho + \Lambda &= 3\dot\alpha^2 - e^{-2\alpha}\left[2\nabla^2\alpha + (\nabla\alpha)^2\right] \\ &= 3\dot\alpha^2 + \tfrac{1}{2}\,{}^{(3)}\!R, \qquad (24)\\ 8\pi G\, q_i &= 2\,\partial_i\dot\alpha, \qquad (25)\\ 8\pi G\, p - \Lambda &= -\left(2\ddot\alpha + 3\dot\alpha^2\right) + \tfrac{1}{3}e^{-2\alpha}\left[2\nabla^2\alpha + (\nabla\alpha)^2\right] \\ &= -\left(2\ddot\alpha + 3\dot\alpha^2\right) - \tfrac{1}{6}\,{}^{(3)}\!R, \qquad (26)\\ 8\pi G\,\pi^i{}_j &= e^{-2\alpha}\Big[\partial_i\alpha\,\partial_j\alpha - \partial_i\partial_j\alpha \\ &\quad - \tfrac{1}{3}\delta_{ij}\left((\nabla\alpha)^2 - \nabla^2\alpha\right)\Big]. \qquad (27) \end{aligned}$$

Here q_i are covariant components; the physical magnitude is $|q| = (h^{ij}q_iq_j)^{1/2} = e^{-\alpha}|\partial\dot\alpha|/(4\pi G)$. Equation (27) is the trace-free part of $-{}^{(3)}\!R_{ij}$, i.e. $8\pi G\,\pi_{ij} = -{}^{(3)}\!R_{\langle ij\rangle}$, where angle brackets denote the projected symmetric trace-free part.

Two features of Eqs. (24)–(27) drive everything that follows. First, the energy flux is the gradient of the local Hubble rate, $8\pi G q_i = 2\partial_i\mathcal{H}$: a spatially varying expansion rate implies a flow of energy relative to the comoving observers. Second, the anisotropic stress is fixed entirely by the spatial geometry: it vanishes only if the trace-free spatial Ricci tensor vanishes.

C. Constraint equations

Equation (24) is the Hamiltonian constraint,

$${}^{(3)}\!R + \tfrac{2}{3}\theta^2 - 2\sigma^2 = 16\pi G\rho + 2\Lambda, \qquad (28)$$

with $\sigma^2 = 0$. Equation (25) is the momentum constraint,

$$D^b\sigma_{ab} - \tfrac{2}{3}D_a\theta + \varepsilon_{abc}D^b\omega^c = -8\pi G\, q_a, \qquad (29)$$

which with Eq. (21) reduces to $-2D_a\dot\alpha = -8\pi G q_a$, in agreement with Eq. (25). The remaining constraints of the $1+3$ system [54],

$$\begin{aligned} \operatorname{curl}\sigma_{ab} + D_{\langle a}\omega_{b\rangle} &= H_{ab}, \qquad (30)\\ D^bE_{ab} - \tfrac{8\pi G}{3}D_a\rho & \\ +4\pi G\left(D^b\pi_{ab} + \tfrac{2}{3}\theta q_a\right) &= 0, \qquad (31) \end{aligned}$$

fix the magnetic Weyl tensor and the divergence of the electric Weyl tensor.

D. Weyl curvature

The shear propagation equation of the $1+3$ formalism reads

$$\begin{aligned} &\dot\sigma_{\langle ab\rangle} + \tfrac{2}{3}\theta\sigma_{ab} + \sigma_{c\langle a}\sigma_{b\rangle}{}^c + \omega_{\langle a}\omega_{b\rangle} \\ &\quad - D_{\langle a}A_{b\rangle} - A_{\langle a}A_{b\rangle} + E_{ab} - 4\pi G\,\pi_{ab} = 0. \qquad (32) \end{aligned}$$

With $\sigma_{ab} = \omega_{ab} = A_a = 0$ it becomes an algebraic identity:

$$E_{ab} = 4\pi G\,\pi_{ab} = -\tfrac{1}{2}\,{}^{(3)}\!R_{\langle ab\rangle}, \qquad H_{ab} = 0. \qquad (33)$$

The Weyl tensor is purely electric and is determined by the trace-free spatial curvature. We confirmed Eq. (33) by computing C_{i0j0} directly from the metric for a test function $\alpha(t,\mathbf{x})$. The Weyl invariant is

$$C_{abcd}C^{abcd} = 8\left(E_{ab}E^{ab} - H_{ab}H^{ab}\right) = 8(4\pi G)^2\pi_{ab}\pi^{ab}. \qquad (34)$$

Tidal fields around a void are thus in one-to-one correspondence with the anisotropic stress the geometry requires.

E. Evolution and conservation equations

The Raychaudhuri equation for the comoving congruence is

$$\dot\theta + \tfrac{1}{3}\theta^2 = -4\pi G\,(\rho + 3p) + \Lambda, \qquad (35)$$

and with Eqs. (24) and (26) it reduces to $3(\ddot\alpha + \dot\alpha^2) = 3\ddot R_{\rm eff}/R_{\rm eff}$ with $R_{\rm eff} = e^\alpha$, i.e. it holds identically. The contracted Bianchi identity $\nabla_a T^{ab} = 0$ yields the energy and momentum equations [54]

$$\begin{aligned} \dot\rho + \theta(\rho + p) + D_aq^a + 2A_aq^a + \sigma_{ab}\pi^{ab} &= 0, \qquad (36)\\ \dot q_{\langle a\rangle} + \tfrac{4}{3}\theta q_a + \sigma_{ab}q^b - \varepsilon_{abc}\omega^bq^c & \\ +(\rho + p)A_a + D_ap + D^b\pi_{ab} + A^b\pi_{ab} &= 0. \qquad (37) \end{aligned}$$

For our congruence they simplify to

$$\begin{aligned} \dot\rho + 3\dot\alpha\,(\rho + p) + e^{-3\alpha}\partial_i(e^\alpha q_i) &= 0, \qquad (38)\\ \dot q_{\langle i\rangle} + 4\dot\alpha\, q_i + \partial_ip + D^j\pi_{ij} &= 0, \qquad (39) \end{aligned}$$

which are satisfied identically by Eqs. (24)–(27). Equation (38) shows that in the comoving frame density can change through divergence of the energy flux as well as through expansion. This will matter when we interpret void evolution (Sec. V C).

F. A uniqueness theorem

Theorem 1. *For the metric (3), the energy–momentum tensor is that of a perfect fluid comoving with u^a ($q_a = 0$, $\pi_{ab} = 0$) if and only if the spacetime is FLRW, i.e. $\alpha = \ln a(t) - \ln\left(c_0 + c_ix^i + \frac{1}{4}k\,|\mathbf{x}|^2\right)$ with constants c_0, c_i and k, which is FLRW in translated and rescaled coordinates.*

Proof. If $q_i = 0$, Eq. (25) gives $\partial_i\dot\alpha = 0$, so $\alpha = \ln a(t) + \beta(\mathbf{x})$. If $\pi_{ij} = 0$, Eq. (27) requires the trace-free part of $\partial_i\partial_j\beta - \partial_i\beta\,\partial_j\beta$ to vanish. With $\phi \equiv e^{-\beta}$ one has $\partial_i\partial_j\phi = -\phi\,(\partial_i\partial_j\beta - \partial_i\beta\,\partial_j\beta)$, so $\partial_i\partial_j\phi = \lambda(\mathbf{x})\delta_{ij}$. The integrability condition $\partial_k\partial_i\partial_j\phi = \partial_i\partial_k\partial_j\phi$ gives $\delta_{ij}\partial_k\lambda = \delta_{kj}\partial_i\lambda$, so in three dimensions λ is constant. Integrating, $\phi = c_0 + c_ix^i + \frac{1}{2}\lambda|\mathbf{x}|^2$, and the spatial metric $\phi^{-2}\delta_{ij}$ has constant curvature. The converse is immediate. □

Corollary 1. *A void, or any inhomogeneity, in the metric (3) requires an energy flux, an anisotropic stress, or both. If the scale factor separates, $R = a(t)e^{\psi(\mathbf{x})}$, the flux vanishes and the inhomogeneity is supported entirely by anisotropic stress and an inhomogeneous isotropic pressure.*

Theorem 1 is a special case of results on shear-free perfect fluids [46, 56]: geodesic, shear-free, irrotational perfect-fluid flows with an equation of state are FLRW. In the rest of the paper we therefore regard Eqs. (24)–(27) as defining an *effective* fluid. Possible physical interpretations are discussed in Sec. XII C.

G. Energy conditions

When $q_a = 0$, the eigenvalues of $T^a{}_b$ are $-\rho$ and the principal pressures $p_I = p+\pi_I$, where π_I are the eigenvalues of $\pi^i{}_j$. The weak, null, strong and dominant energy conditions [57] become

$$\text{WEC:}\quad \rho \geq 0,\quad \rho + p_I \geq 0; \qquad \text{NEC:}\quad \rho + p_I \geq 0; \tag{40}$$

$$\text{SEC:}\quad \rho + p_I \geq 0,\quad \rho + 3p \geq 0; \qquad \text{DEC:}\quad \rho \geq |p_I|. \tag{41}$$

Since $\rho + 3p = -(3/4\pi G)(\ddot{\alpha} + \dot{\alpha}^2)$ by Eq. (35) (with $\Lambda = 0$), the SEC fails wherever the local expansion accelerates. When $q_a \neq 0$, the conditions involve the eigenvalues of the full 4×4 matrix $T^a{}_b$; for $|q| \ll \rho$ they hold if $\rho + p_I > 2|q|$ to leading order. We evaluate the conditions for explicit voids in Sec. VI C.

IV. LIGHT PROPAGATION: REDSHIFT, DISTANCES AND LENSING

A. Redshift

Let $k^a = dx^a/d\lambda$ be the tangent to a null geodesic. The time component of the geodesic equation with Eq. (6) gives

$$\frac{dk^0}{d\lambda} + \dot{\alpha}\, e^{2\alpha}\delta_{ij}k^i k^j = 0 \implies \frac{dk^0}{d\lambda} = -\dot{\alpha}\,(k^0)^2, \tag{42}$$

using the null condition $e^{2\alpha}\delta_{ij}k^i k^j = (k^0)^2$. Since $dt = k^0 d\lambda$, $d\ln k^0/dt = -\dot{\alpha}(t, \mathbf{x}(t))$ along the ray. The redshift measured by comoving observers, $1 + z = (u_a k^a)_e/(u_a k^a)_o = k^0_e/k^0_o$, is therefore

$$\begin{aligned} 1 + z &= \exp\left[\int_{t_e}^{t_o} \dot{\alpha}\big(t, \mathbf{x}(t)\big)\, dt\right] \\ &= \frac{R_{\rm eff}(t_o, \mathbf{x}_o)}{R_{\rm eff}(t_e, \mathbf{x}_e)} \exp\left[-\int_{\mathbf{x}_e}^{\mathbf{x}_o} \nabla\alpha \cdot d\mathbf{x}\right], \end{aligned} \tag{43}$$

where the second form uses $d\alpha/dt = \dot{\alpha} + \nabla\alpha \cdot d\mathbf{x}/dt$ along the ray. For $\alpha = \ln a + \psi$,

$$\ln(1 + z) = \ln\frac{a_o}{a_e} + \int_{t_e}^{t_o} \dot{\psi}\, dt. \tag{44}$$

A static spatial factor ($\dot{\psi} = 0$) leaves the redshift–time relation exactly that of the background: there is neither a Sachs–Wolfe nor an integrated Sachs–Wolfe effect, and no peculiar redshift for comoving sources. A time-dependent ψ produces an ISW-like shift

$$\frac{\Delta T}{T} = -\int \dot{\psi}\, dt. \tag{45}$$

B. Optical equivalence and lensing

Null geodesics are conformally invariant up to affine reparametrization. Writing the metric with $\alpha = \ln a + \psi$ and conformal time $d\eta = dt/a$,

$$ds^2 = a^2 e^{2\psi}\left[-e^{-2\psi}d\eta^2 + \delta_{ij}dx^i dx^j\right], \tag{46}$$

the light rays are those of the optical metric $-e^{-2\psi}d\eta^2 + d\mathbf{x}^2$, i.e. of a medium with refractive index $n = e^{\psi}$. Compare the linearly perturbed FLRW metric in the Newtonian gauge,

$$\begin{aligned} ds^2 &= a^2\left[-(1 + 2\Phi)d\eta^2 + (1 - 2\Psi)\delta_{ij}dx^i dx^j\right] \\ &\simeq a^2(1 - 2\Psi)\left[-(1 + 2\Phi + 2\Psi)d\eta^2 + d\mathbf{x}^2\right], \end{aligned} \tag{47}$$

in which lensing depends only on $\Phi + \Psi$ [58]. Matching Eq. (46) to linear order gives

$$(\Phi + \Psi)_{\rm model} = -\psi. \tag{48}$$

The deflection angle and convergence are

$$\begin{aligned} \hat{\boldsymbol{\alpha}} &= 2\int \nabla_\perp \psi\, d\chi \quad \text{(model)}, \\ \kappa &= -\int_0^{\chi_s} \frac{\chi(\chi_s - \chi)}{\chi_s}\, \nabla_\perp^2 \psi\, d\chi. \end{aligned} \tag{49}$$

In Sec. V we show that at linear order $\psi = -\Phi_N/c^2$, where Φ_N is the Newtonian potential sourced by the density contrast. General relativity with $\Phi = \Psi = \Phi_N$ gives $(\Phi + \Psi)_{\rm GR} = 2\Phi_N$, whereas the model gives Φ_N. *At fixed density, the model lenses exactly half as strongly as general relativity.*

C. Angular-diameter and luminosity distances

The area distance d_A of a thin beam obeys the Sachs focusing equation [59],

$$\begin{aligned} \frac{d^2\sqrt{A}}{d\lambda^2} &= -\left(\tfrac{1}{2}R_{ab}k^a k^b + |\hat{\sigma}|^2\right)\sqrt{A}, \\ \frac{R_{ab}k^a k^b}{8\pi G} &= (\rho + p)(u \cdot k)^2 - 2(u \cdot k)\, q_a k^a + \pi_{ab}k^a k^b, \end{aligned} \tag{50}$$

where $\hat{\sigma}$ is the optical shear, sourced by the Weyl tensor, i.e. by $E_{ab} = 4\pi G\pi_{ab}$. The energy flux and anisotropic stress thus focus light in addition to $\rho + p$. The luminosity distance follows from Etherington's reciprocity theorem [60], $d_L = (1+z)^2 d_A$, which holds for any metric theory with photon conservation [61].

V. RELATION TO PERTURBATION THEORY AND CLOSURES

A. Linearization

Write $\alpha = \ln a(t) + \psi(t,\mathbf{x})$ with $|\psi| \ll 1$, and restore c. To first order, Eqs. (24)–(27) give

$$8\pi G\,\delta\rho = 6H\dot{\psi} - \frac{2c^2}{a^2}\nabla^2\psi, \tag{51}$$

$$8\pi G\,q_i = 2c\,\partial_i\dot{\psi}, \tag{52}$$

$$8\pi G\,\delta p = -2\ddot{\psi} - 6H\dot{\psi} + \frac{2c^2}{3a^2}\nabla^2\psi, \tag{53}$$

$$8\pi G\,\pi^i{}_j = -\frac{c^2}{a^2}\left(\partial_i\partial_j - \tfrac{1}{3}\delta_{ij}\nabla^2\right)\psi, \tag{54}$$

with $H = \dot{a}/a$ and the background obeying the Friedmann equations. For matter-dominated structure we define $\delta \equiv \delta\rho/\bar{\rho}_m$ with $8\pi G\bar{\rho}_m = 3\Omega_m H_0^2 a^{-3}$.

B. Gauge comparison and Bardeen potentials

In conformal time Eq. (3) reads, to first order, $ds^2 = a^2[-d\eta^2 + (1+2\psi)d\mathbf{x}^2]$. In the notation of Refs. [36, 38],

$$ds^2 = a^2\Big[-(1+2\phi)d\eta^2 + 2\partial_i B\,d\eta\,dx^i + ((1-2\psi_M)\delta_{ij} + 2\partial_i\partial_j E)\,dx^i dx^j\Big], \tag{55}$$

we have $\phi = B = E = 0$ and $\psi_M = -\psi$. The Bardeen potentials,

$$\Phi_B = \phi + \frac{1}{a}\left[a(B-E')\right]', \qquad \Psi_B = \psi_M - \mathcal{H}_c(B-E'), \tag{56}$$

with $\mathcal{H}_c = a'/a$, are therefore

$$\Phi_B = 0, \qquad \Psi_B = -\psi. \tag{57}$$

The metric (3) is the Newtonian gauge with the time–time potential switched off. In synchronous gauge [39], $h_{ij} = \hat{k}_i\hat{k}_j h + (\hat{k}_i\hat{k}_j - \frac{1}{3}\delta_{ij})6\eta_s$, it corresponds to $h = 6\psi$ and $\eta_s = -\psi$ with the traceless longitudinal part tied to the trace. A general synchronous perturbation has two independent scalar functions; here only one survives, which is why an anisotropic stress is required.

In the language of phenomenological modified gravity [62, 63], with $k^2\Psi_B = -4\pi G a^2\mu\,\bar{\rho}\Delta$ and $k^2(\Phi_B + \Psi_B) = -8\pi G a^2\Sigma\,\bar{\rho}\Delta$, Eq. (57) corresponds to an infinite gravitational slip Ψ_B/Φ_B, to no gravitational acceleration of comoving matter ($\Phi_B = 0$), and to

$$\Sigma = \tfrac{1}{2}. \tag{58}$$

C. Closures

Equations (51)–(54) hold for any $\psi(t,\mathbf{x})$; they determine the effective source once ψ is specified. Dynamics needs an additional assumption. We consider three.

a. (i) Static closure. Take $\psi = \psi(\mathbf{x})$, i.e. $R = a(t)e^{\psi(\mathbf{x})}$. Then $q_i = 0$. Exactly, not only at linear order, Eqs. (24) and (26) give

$$8\pi G\,\delta\rho = -\frac{c^2}{a^2}e^{-2\psi}\left[2\nabla^2\psi + (\nabla\psi)^2\right], \quad \delta p = -\tfrac{1}{3}\delta\rho\,c^2, \tag{59}$$

where $\delta\rho$ and δp are measured from the background ΛCDM values. The inhomogeneity is carried by a component with equation of state $w = -1/3$, the equation of state of spatial curvature in FLRW, which dilutes as a^{-2}. Relative to the matter density ($\propto a^{-3}$),

$$\delta(t,\mathbf{x}) = \frac{a}{a_0}\,\delta(t_0,\mathbf{x}) \;\Rightarrow\; D_{\rm static} = a, \quad f \equiv \frac{d\ln D}{d\ln a} = 1, \tag{60}$$

for any background, including ΛCDM. In a matter-dominated universe this coincides with the linear growing mode, but there is no Λ suppression at late times. Normalized to the same early-time amplitude, $D_{\rm static}/D_{\Lambda\rm CDM} = 1.27$ at $z = 0$, so the model has $\sigma_8 = 1.03$ when ΛCDM has 0.811 (Table I). Moreover, because $q_i = 0$ the effective fluid has no peculiar motion relative to u^a: *the static closure predicts no redshift-space distortion.* Equation (38) confirms that the density contrast grows without any flow, through the $w = -1/3$ pressure.

b. (ii) Pressureless closure. Setting $\delta p = 0$ in Eq. (53) gives

$$\ddot{\psi} + 3H\dot{\psi} = \frac{c^2}{3a^2}\nabla^2\psi \quad\Longrightarrow\quad \ddot{\psi}_k + 3H\dot{\psi}_k + \frac{c^2k^2}{3a^2}\psi_k = 0, \tag{61}$$

a wave equation with sound speed $c_s = c/\sqrt{3}$. Modes with $k \gtrsim aH\sqrt{3}/c$, i.e. wavelengths shorter than about $1.7\,h^{-1}$ Gpc today, oscillate instead of growing (Fig. 2). Since all observed voids are far smaller than this, the pressureless closure cannot describe them.

c. (iii) Growth-matched closure. Take $\psi(t,\mathbf{x}) = A(t)\psi_0(\mathbf{x})$ and choose A so that δ follows linear ΛCDM. For sub-horizon modes the $6H\dot{\psi}$ term in Eq. (51) is suppressed by $(aH/ck)^2$, so

$$A(a) = \frac{D_{\Lambda\rm CDM}(a)}{a\,D_{\Lambda\rm CDM}(1)}, \tag{62}$$

so that $A(1) = 1$, $A(0.5) = 1.15$ and $A(0.33) = 1.25$. Now $\dot{\psi} \neq 0$ at late times: there is an energy flux [Eq. (52)]

and an ISW-like effect [Eq. (45)]. In the energy frame the effective fluid moves with velocity $\boldsymbol{v} = \boldsymbol{q}/\bar{\rho}$, i.e.

$$\boldsymbol{v} = \frac{2c^2a^3}{3\Omega_m H_0^2}\,\nabla\dot{\psi} \overset{a=1}{=} \frac{2c^2(f-1)}{3\Omega_m H_0}\,\nabla\psi. \tag{63}$$

For comparison, linear ΛCDM has $\boldsymbol{v} = -(2f/3\Omega_m H_0)\nabla\Phi_N = (2fc^2/3\Omega_m H_0)\nabla\psi$. The two differ in sign, and in magnitude by $(1-f)/f = 0.90$ at $z = 0$. The model predicts energy flowing *into* voids at late times, whereas galaxies flow out of them.

D. Covariant gradient formulation

The growth laws of the closures can also be derived without coordinates, using the comoving gradient variables of the $1+3$ formalism [54, 55],

$$\Delta_a \equiv \frac{a}{\rho}D_a\rho, \qquad \mathcal{Z}_a \equiv a\,D_a\theta. \tag{64}$$

Taking the spatial gradient of the energy equation (36) and of the Raychaudhuri equation (35), and linearizing about FLRW with $A_a = \sigma_{ab} = \omega_{ab} = 0$, gives

$$\dot{\Delta}_a = w\theta\Delta_a - (1+w)\mathcal{Z}_a - \frac{a\theta}{\rho}D_a p - \frac{a}{\rho}D_a D^b q_b, \tag{65}$$

$$\dot{\mathcal{Z}}_a = -\tfrac{2}{3}\theta\mathcal{Z}_a - 4\pi G\rho\,\Delta_a - 12\pi G\,aD_a p, \tag{66}$$

where $w = p/\rho$ is the background equation of state. In general relativity with dust ($p = q = 0$), eliminating $\mathcal{Z}_a$ yields the familiar $\ddot{\Delta}_a + 2H\dot{\Delta}_a - 4\pi G\rho\Delta_a = 0$. In the static closure, $\theta = 3H$ is uniform, so $\mathcal{Z}_a = 0$ identically and Eq. (66) becomes the *constraint*

$$aD_a p = -\tfrac{1}{3}\rho\,\Delta_a, \tag{67}$$

which is the gradient form of $\delta p = -\delta\rho/3$. Substituting into Eq. (65) with $w = 0$ for the matter background gives $\dot{\Delta}_a = H\Delta_a$, i.e. $\Delta \propto a$, independently of the background expansion history. This reproduces Eq. (60) covariantly. The pressure gradient of the curvature fluid, not gravity, drives the growth.

E. Primordial origin of the conformal factor

In the matter era the comoving curvature perturbation ζ of single-field inflation [38] fixes the Newtonian-gauge potentials, $\Phi = \Psi = -\frac{3}{5}\zeta$. With Eq. (57) this gives

$$\psi = \tfrac{3}{5}\,\zeta, \qquad \Delta^2_\psi(k) = \tfrac{9}{25}A_s\left(\frac{k}{k_*}\right)^{n_s-1} \tag{68}$$

on scales that entered the horizon in the matter era. With $A_s = 2.1\times10^{-9}$ [70] the rms conformal factor per logarithmic interval is 2.7×10^{-5}, consistent with $\psi_{\rm rms} = 2.1\times10^{-5}$ in our mocks. In this sense the spatially varying scale factor is the large-scale curvature perturbation itself, frozen into the spatial metric. Primordial non-Gaussianity of local type, $\zeta = \zeta_G + \frac{3}{5}f_{\rm NL}(\zeta_G^2 - \langle\zeta_G^2\rangle)$, gives the static-closure density a skewness of order $f_{\rm NL}\psi_{\rm rms} \sim 10^{-4}$ for $|f_{\rm NL}| \lesssim 5$ [70]. This is negligible compared with $S_3 \approx 3$ (Sec. X D).

F. Growth rate and the E_G statistic

Table I and Fig. 1 compare the growth functions. The static closure has $f = 1$ at all redshifts, against $f_{\Lambda\rm CDM}(0) = 0.53$. A lensing-to-velocity statistic [63, 64] isolates the slip:

$$E_G = \frac{\nabla^2(\Phi_B + \Psi_B)}{3H_0^2 a^{-1} f\,\delta} = \frac{2\,\Omega_m\Sigma}{f},$$

$$E_G^{\Lambda\rm CDM} = \frac{\Omega_m}{f}, \quad E_G^{\rm static} = \frac{\Omega_m}{2}, \quad E_G^{\rm g.m.} = \frac{\Omega_m}{2f}. \tag{69}$$

At $z = 0.32$ these are 0.45, 0.16 and 0.23 for $\Omega_m = 0.315$. The measured value at this redshift, $E_G = 0.39 \pm 0.06$ [64], is consistent with ΛCDM and lies about 3.9σ and 2.7σ above the two closures. Note that the static closure, having no peculiar velocities, would in fact predict no velocity signal at all; Eq. (69) assumes that velocities are measured through some other tracer.

VI. VOIDS AS DOMAINS OF NEGATIVE SPATIAL CURVATURE

A. The Lichnerowicz equation

Using the identity (18) in Eq. (24), the Hamiltonian constraint for the static closure at time t becomes, with $w \equiv e^{\psi/2}$,

$$\nabla^2 w = -\frac{3\Omega_m H_0^2}{4c^2 a}\,\delta(\mathbf{x})\,w^5 = -2\pi G\,a^2\,\delta\rho\,w^5/c^2. \tag{70}$$

This is the Lichnerowicz equation of the conformal method for the initial-value problem of general relativity [65, 66], here with the time-symmetric part replaced by the background expansion. It is semilinear and, for $\delta \geq -1$ and suitable boundary conditions, has a unique positive solution. Any observed or simulated void profile $\delta(r)$ can therefore be converted into an exact conformal factor $\psi(r) = 2\ln w(r)$. The local curvature follows from Eq. (59):

$${}^{(3)}R = \frac{16\pi G}{c^2}\,\delta\rho = \frac{6\Omega_m H_0^2}{c^2 a^3}\,\delta, \qquad \Omega_k^{\rm loc} = -\Omega_m(a)\,\delta. \tag{71}$$

In the static closure the local curvature is *exactly* proportional to the density contrast. Voids ($\delta < 0$) are locally open ($\Omega_k^{\rm loc} > 0$), and overdense walls are locally closed.

TABLE I. Linear growth function $D(z)$ (normalized to $D \to a$ at early times) and growth rate f for ΛCDM ($\Omega_m = 0.315$) and for the static closure of Eq. (60). The last column is the ratio of amplitudes for equal primordial normalization.

z	$D_{\Lambda\mathrm{CDM}}$	D_{static}	$f_{\Lambda\mathrm{CDM}}$	f_{static}	$D_{\mathrm{static}}/D_{\Lambda\mathrm{CDM}}$	$A(z)$ [Eq. (62)]
0	0.788	1.000	0.527	1	1.269	1.000
0.25	0.690	0.800	0.662	1	1.160	1.10
0.5	0.606	0.667	0.761	1	1.101	1.15
0.75	0.536	0.571	0.830	1	1.067	1.19
1	0.478	0.500	0.877	1	1.046	1.21
2	0.329	0.333	0.959	1	1.014	1.25
3	0.248	0.250	0.982	1	1.006	1.26

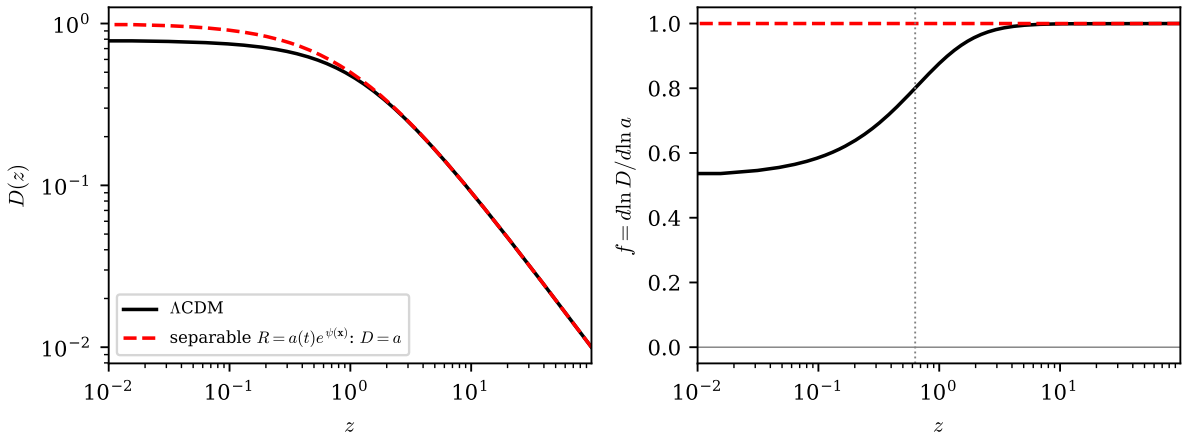


FIG. 1. Left: linear growth function for ΛCDM (solid) and for the static closure $R = a(t)e^{\psi(\mathbf{x})}$ (dashed), for which $D = a$ exactly. Right: growth rate $f = d\ln D/d\ln a$. The vertical dotted line marks the onset of acceleration, $z = 0.63$.

B. A spherical void

For a spherical void, Eq. (70) reduces to the ordinary differential equation

$$w'' + \frac{2}{r}\,w' = -\frac{3\Omega_m H_0^2}{4c^2}\,\delta(r)\,w^5, \qquad w(0) = 1,\ w'(0) = 0, \tag{72}$$

which we integrate outward and then normalize so that $\psi \to 0$ as $r \to \infty$. For the density profile we use the universal form of Hamaus, Sutter and Wandelt (HSW) [17],

$$\delta(r) = \delta_c\,\frac{1-(r/r_s)^{\alpha_v}}{1+(r/r_v)^{\beta_v}}, \tag{73}$$

with the representative parameters $\delta_c = -0.85$, $r_v = 30\,h^{-1}\,\mathrm{Mpc}$, $r_s = 0.91\,r_v$, $\alpha_v = 2$ and $\beta_v = 9$. The resulting fields are shown in Fig. 3 and summarized in Table II.

The conformal factor has a minimum at the void centre, with depth

$$\psi(0) = -4.8 \times 10^{-6}. \tag{74}$$

This is the same order as the Newtonian potential of the void divided by c^2, as Eq. (57) requires. The nonlinear terms $(\nabla\psi)^2$ and $e^{-2\psi}$ in Eq. (59) are therefore negligible at the 10^{-5} level even in a void that is 85% empty: the large density contrast comes from the *curvature* of the conformal factor, not from its amplitude. The local curvature parameter at the centre is $\Omega_k^{\mathrm{loc}} = 0.27$, corresponding to a curvature radius $c/(H_0\sqrt{\Omega_k^{\mathrm{loc}}}) = 5.8\,h^{-1}\,\mathrm{Gpc}$. Around $r \simeq r_v$ the compensating overdense ridge is locally closed.

For a uniform underdense sphere of radius R and contrast δ, Eq. (72) gives, to leading order,

$$\psi(0) - \psi(R) = \frac{\Omega_m}{4}\,|\delta|\left(\frac{H_0 R}{c}\right)^2, \tag{75}$$

so even the largest reported underdensities, $R \sim 200\,h^{-1}\,\mathrm{Mpc}$ with $|\delta| \sim 0.1$–0.3 [21, 22], require $|\psi| \sim 10^{-4}$ (Table III).

C. Stresses and energy conditions

For spherical symmetry the anisotropic stress has eigenvalues $\pi^r{}_r = -2\pi^\theta{}_\theta$, with [Eq. (27)]

$$8\pi G\left(\pi^r{}_r - \pi^\theta{}_\theta\right) = \frac{c^2}{a^2}e^{-2\psi}\left[\psi'^2 - \psi'' + \frac{\psi'}{r}\right]. \tag{76}$$

The isotropic pressure of the curvature component is $p_\psi = -\delta\rho\,c^2/3$, positive inside the void. Figure 3(d)

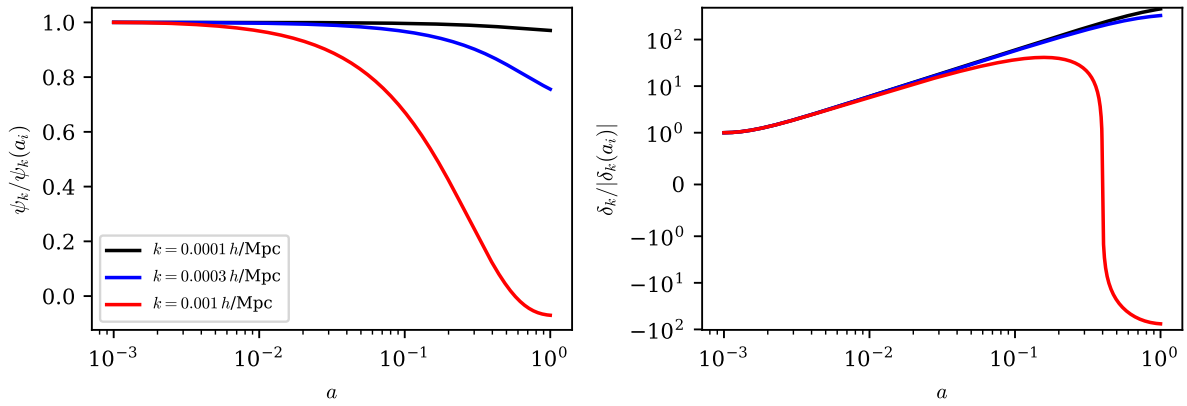


FIG. 2. Pressureless closure, Eq. (61): evolution of ψ_k (left) and of the density contrast from Eq. (51) (right) for three very long wavelengths. Already at $k = 10^{-3}\,h\,\mathrm{Mpc}^{-1}$ the mode oscillates; void-scale modes ($k \sim 0.1$) oscillate thousands of times per Hubble time.

shows that the stress anisotropy reaches 17% of $\bar{\rho}_m c^2$ near the void edge. The weak energy condition, evaluated with the principal pressures, holds everywhere: its most restrictive combination has a minimum of $0.15\,\bar{\rho}_m$, attained by ρ itself at the centre. In the static closure the central density contrast grows as a, so this void would reach $\rho = 0$ at $a = 1/0.85$; beyond that the effective source violates the WEC. This is the static-closure analogue of the emptying of voids in the spherical model [30].

D. Lensing and ISW signatures

The convergence profile of the void at $z_l = 0.3$ for sources at $z_s = 1$ is shown in Fig. 4. In general relativity the central convergence is $\kappa_0 = -9.9\times10^{-4}$ and the tangential shear peaks at $\gamma_t = -4.9\times10^{-4}$ near $R_\perp \simeq 0.9 r_v$. The model predicts exactly half of both, by Eq. (48). Stacked void lensing [67, 68] can therefore test the model directly.

For the growth-matched closure, the ISW-like shift of a photon crossing the void centre is $\Delta T/T = -\psi(0)\,\Delta A$, against $2\Delta(\Phi_N/c^2)$ in general relativity. Since $\Phi_N/c^2 = -\psi$ has the same time dependence $A(a)$, the model gives the same sign as general relativity (a cold spot behind a void) and half the amplitude: -4.0×10^{-8} against -8.0×10^{-8} at $z_c = 0.1$ for this void (Fig. 5). The static closure gives no ISW signal at all.

VII. COMPARISON WITH AN EXACT LEMAÎTRE–TOLMAN–BONDI VOID

The static closure grows density contrasts as $D = a$, which in an Einstein–de Sitter (EdS) background is the growing mode of linear theory. It is therefore exact only while $|\delta| \ll 1$. To quantify how this compares with the nonlinear evolution of a real void, we evolve the same initial profile in an exact spherically symmetric dust solution, the LTB model [41–43].

A. The LTB void

In comoving coordinates the LTB metric is

$$ds^2 = -dt^2 + \frac{\mathcal{R}'^2(t,r)}{1+2\mathcal{E}(r)}\,dr^2 + \mathcal{R}^2(t,r)\,d\Omega^2, \qquad (77)$$

where each shell obeys the Friedmann-like equation and the density follows from mass conservation:

$$\dot{\mathcal{R}}^2 = \frac{2GM(r)}{\mathcal{R}} + 2\mathcal{E}(r), \qquad 4\pi G\rho = \frac{GM'}{\mathcal{R}^2\mathcal{R}'}. \qquad (78)$$

At $a_i = 10^{-3}$ we set $\mathcal{R} = a_i r$, choose $M(r) = \frac{4}{3}\pi\bar{\rho}_i(1+\bar{\Delta}_i)r^3 a_i^3$ with $\bar{\Delta}_i(r)$ the mean contrast within r, and give each shell the growing-mode velocity

$$\dot{\mathcal{R}}_i = H_i\mathcal{R}_i\left(1 - \tfrac{1}{3}\bar{\Delta}_i\right). \qquad (79)$$

The energy $\mathcal{E}(r)$ then follows from Eq. (78), and each shell is integrated independently to $a = 1$. The initial profile is the HSW form (73), scaled so that its linear extrapolation to $a = 1$ has central value $\delta_{\rm lin}(0) = -1$, -2 or -3. Distances are in units of r_v; the evolution is self-similar in amplitude, so $\delta_{\rm lin}(0) = -2$ at $a = 0.5$ reproduces $\delta_{\rm lin}(0) = -1$ at $a = 1$.

B. Results

Figure 6 and Table IV compare the two evolutions. The LTB void deepens more slowly than linearly and saturates, approaching emptiness asymptotically. For $\delta_{\rm lin}(0) = -2$ at $a = 1$ the exact central contrast is -0.72, while the static closure, which is linear in this

TABLE II. Properties of the spherical void of Sec. VI B (HSW profile, $\delta_c = -0.85$, $r_v = 30\,h^{-1}\,\mathrm{Mpc}$) in the static closure at $z = 0$.

Quantity	Value
Central conformal factor $\psi(0)$	-4.8×10^{-6}
Ratio $(\nabla\psi)^2/\lvert 2\nabla^2\psi\rvert$ (typical)	$\sim 10^{-5}$
Central local curvature Ω_k^{loc}	0.27
Curvature radius at centre	$5.8\,h^{-1}\,\mathrm{Gpc}$
Central curvature-fluid pressure $p_\psi/\bar\rho_m c^2$	0.28
Max. stress anisotropy $\lvert\pi^r{}_r - \pi^\theta{}_\theta\rvert/\bar\rho_m c^2$	0.17
Min. WEC combination$/\bar\rho_m$	0.15
Central convergence κ_0 ($z_l = 0.3$, $z_s = 1$): GR / model	-9.9×10^{-4} / -4.9×10^{-4}
Peak tangential shear γ_t: GR / model	-4.9×10^{-4} / -2.5×10^{-4}
ISW-like $\Delta T/T$ at $z_c = 0.1$: GR / growth-matched	-8.0×10^{-8} / -4.0×10^{-8}

TABLE III. Conformal-factor depth [Eq. (75)] and Gaussian rarity for two large reported underdensities, treated as uniform spheres. δ_L is the linear contrast from the spherical-model mapping $1+\delta = (1-2\delta_L/3)^{-3/2}$ and $\nu = \delta_L/\sigma_L(R)$. Galaxy-based contrasts and radii are approximate, and bias corrections are ignored; the numbers indicate orders of magnitude only.

Region	R [h^{-1} Mpc]	δ	$\lvert\psi\rvert$	$\sigma_L(R)$	ν
KBC-like local underdensity [21]	200	-0.3	1.1×10^{-4}	0.023	-17
Eridanus supervoid [22]	220	-0.14	5.9×10^{-5}	0.020	-8

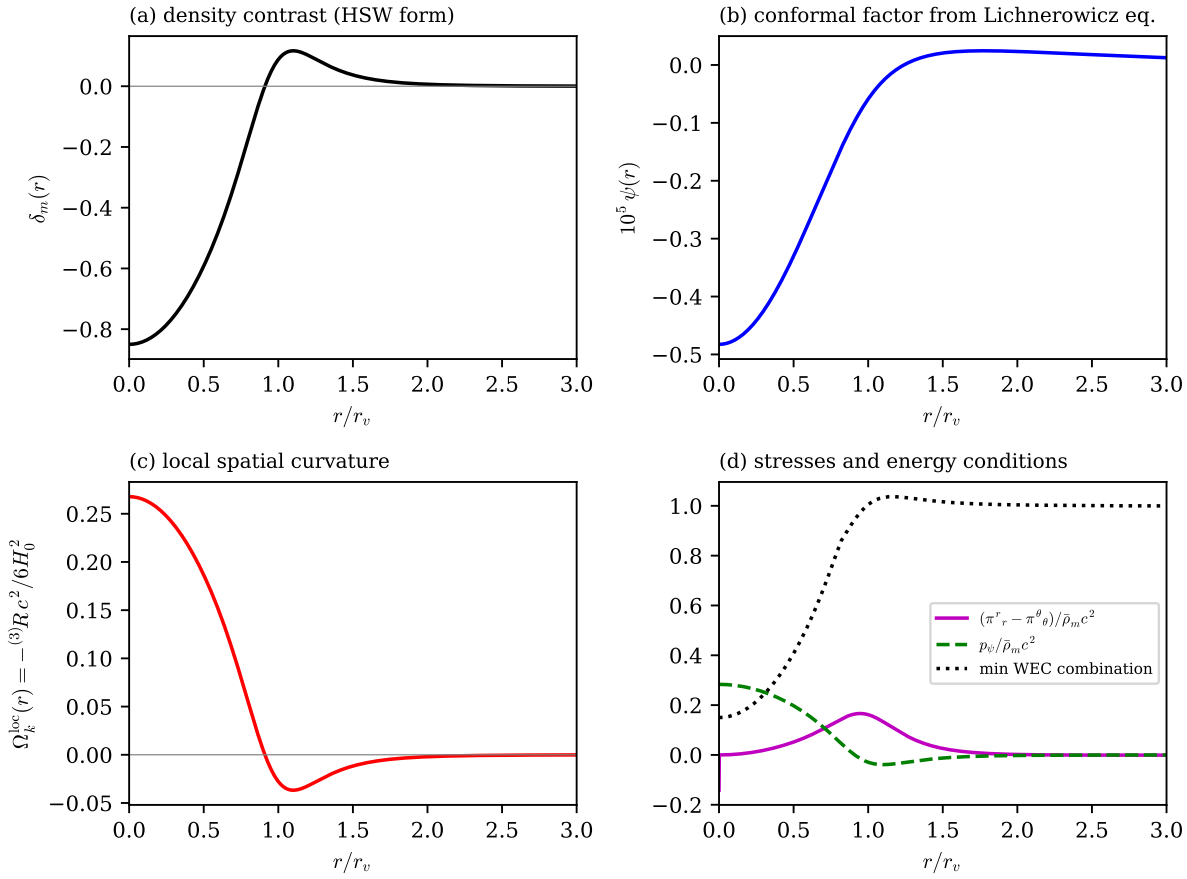


FIG. 3. A spherical void in the static closure. (a) HSW density profile. (b) Conformal factor from the Lichnerowicz equation (72). (c) Local curvature parameter, Eq. (71). (d) Stress anisotropy, isotropic curvature-fluid pressure, and the minimum of the WEC combinations $\{\rho, \rho + p_r, \rho + p_\theta\}$ in units of $\bar\rho_m$.

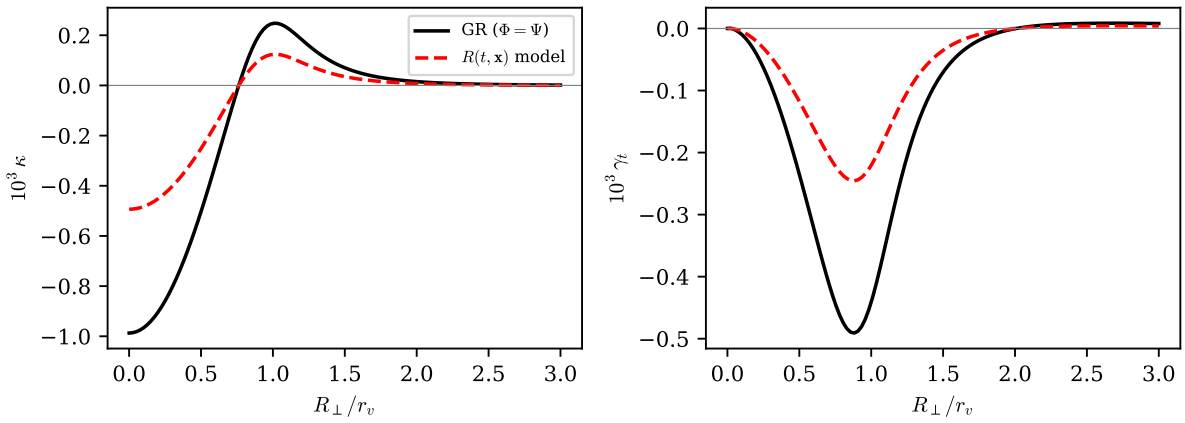


FIG. 4. Convergence (left) and tangential shear (right) of the void of Fig. 3 at $z_l = 0.3$ for sources at $z_s = 1$, in general relativity and in the $R(t, \mathbf{x})$ model. The ratio is exactly 1/2.

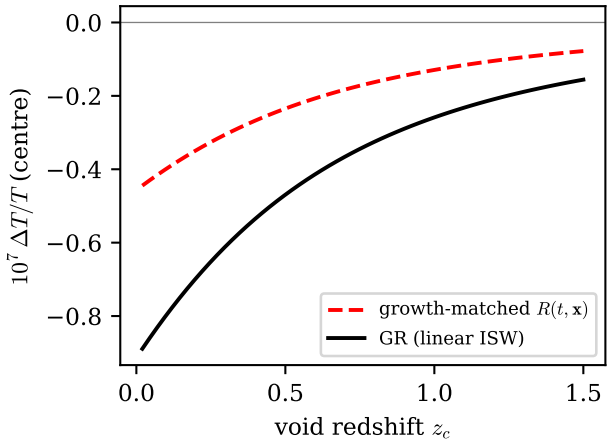


FIG. 5. Central ISW-like temperature shift of the void of Fig. 3 as a function of its redshift, for the growth-matched closure and for linear general relativity (thin-lens estimate).

background, predicts -2, an unphysical negative density. The compensating ridge is enhanced nonlinearly, reaching $\delta = 0.51$ in LTB against 0.27 linearly, approaching but not reaching shell crossing ($\mathcal{R}' > 0$ everywhere for these amplitudes).

The local expansion rates also differ qualitatively. In LTB the transverse and radial Hubble rates at the void centre exceed the background by 29.5% and 27.8% for $\delta_{\rm lin}(0) = -2$. Off centre $H_r \neq H_\perp$, so the void is sheared: near the ridge the radial rate falls to 20% of the background. The static closure has $\mathcal{H} = H$ exactly and no shear [Eq. (21)]. Voids in the real Universe expand faster than the background [18, 30], as in LTB.

TABLE IV. Central and ridge density contrasts and central expansion rates of the exact LTB void compared with the static closure (equal to linear theory in EdS).

$\delta_{\rm lin}(0)$	$\delta^{\rm LTB}(0)$	$\delta^{\rm LTB}_{\rm ridge}$	$\delta^{\rm lin}_{\rm ridge}$	$H_\perp/\bar{H} - 1$	$H_r/\bar{H} - 1$
-0.25	-0.20	0.037	0.034	0.072	0.064
-0.5	-0.34	0.078	0.069	0.127	0.115
-1	-0.53	0.180	0.137	0.205	0.189
-2	-0.72	0.511	0.275	0.295	0.278

C. Geometric comparison

The LTB spatial metric is conformally flat only if $\mathcal{R}'/\sqrt{1+2\mathcal{E}} = \mathcal{R}/r$ up to a conformal factor, which holds only for FLRW. In LTB the electric Weyl tensor is sourced by the difference between the local and mean-enclosed density [47],

$$E^r{}_r = -2E^\theta{}_\theta \propto \rho - \frac{3M}{4\pi\mathcal{R}^3}, \tag{80}$$

whereas in our model $E_{ab} = 4\pi G\pi_{ab}$ is sourced by the anisotropic stress [Eq. (33)]. Both models have $H_{ab} = 0$ in spherical symmetry. The tidal field thus arises from inhomogeneous dust in LTB but from stress in the conformally flat model. This is the geometric counterpart of Theorem 1.

VIII. RESTORING THE LAPSE: THE TWO-FUNCTION METRIC

Sections V–VII trace every observational difficulty of the model to the condition $g_{00} = -1$. We therefore generalize Eq. (3) to

$$ds^2 = -e^{2\nu(t,\mathbf{x})}dt^2 + e^{2\alpha(t,\mathbf{x})}\delta_{ij}\,dx^i dx^j, \tag{81}$$

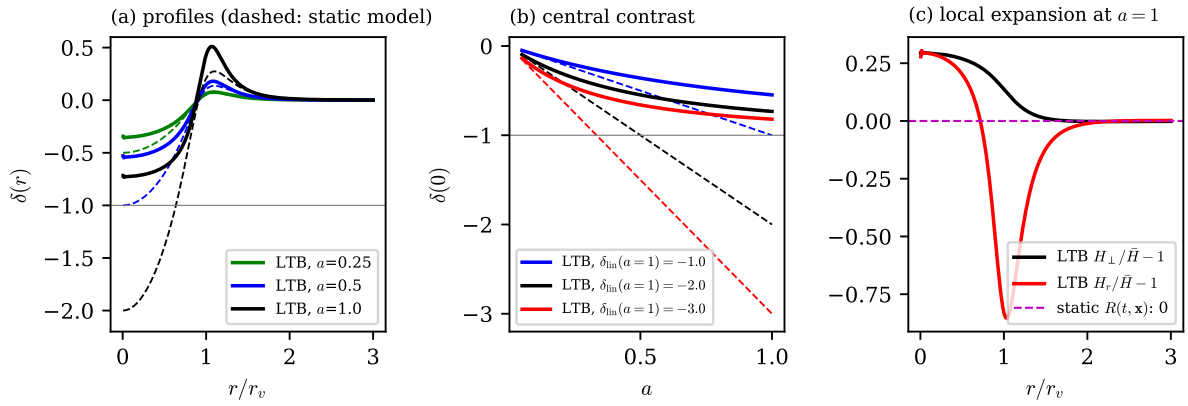


FIG. 6. Exact LTB voids (solid) compared with the static $R(t,\mathbf{x})$ closure (dashed), in an EdS background. (a) Profiles for $\delta_{\rm lin}(0)=-2$ at $a=0.25$, 0.5 and 1. (b) Central contrast as a function of a for three amplitudes. (c) Transverse and radial Hubble rates of the LTB void relative to the background at $a=1$; the static closure has no expansion perturbation.

with lapse $N=e^{\nu}$. This metric contains the Newtonian gauge of cosmological perturbation theory at linear order. It also contains exact solutions such as the Schwarzschild metric in isotropic coordinates and McVittie's metric for a mass embedded in FLRW [82].

A. Einstein tensor

A symbolic computation of the curvature of Eq. (81) for arbitrary α and ν gives

$$G^0{}_0 = -3e^{-2\nu}\dot{\alpha}^2 + e^{-2\alpha}\left[2\nabla^2\alpha + (\nabla\alpha)^2\right], \tag{82}$$

$$G_{0i} = -2\left(\partial_i\dot{\alpha} - \dot{\alpha}\,\partial_i\nu\right), \tag{83}$$

$$G^i{}_j = e^{-2\nu}\left(-2\ddot{\alpha} - 3\dot{\alpha}^2 + 2\dot{\alpha}\dot{\nu}\right)\delta^i_j + e^{-2\alpha}\mathcal{M}_{ij}, \tag{84}$$

with

$$\begin{aligned}\mathcal{M}_{ij} = {}& \partial_i\alpha\,\partial_j\alpha - \partial_i\partial_j\alpha - \partial_i\nu\,\partial_j\nu - \partial_i\partial_j\nu \\ & + \partial_i\alpha\,\partial_j\nu + \partial_j\alpha\,\partial_i\nu \\ & + \delta_{ij}\left[\nabla^2\alpha + \nabla^2\nu + (\nabla\nu)^2\right].\end{aligned} \tag{85}$$

For $\nu=0$ these reduce to Eqs. (13)–(15). The components are given in full in Appendix E.

B. Kinematics and matter content

The observers $u^a = e^{-\nu}\delta^a_0$ now accelerate, with

$$A_a = D_a\nu, \qquad \theta = 3e^{-\nu}\dot{\alpha}, \qquad \sigma_{ab} = \omega_{ab} = 0. \tag{86}$$

The effective fluid has

$$8\pi G\rho + \Lambda = 3e^{-2\nu}\dot{\alpha}^2 + \tfrac{1}{2}{}^{(3)}R, \tag{87}$$

$$8\pi G\, q_i = 2e^{-\nu}\left(\partial_i\dot{\alpha} - \dot{\alpha}\,\partial_i\nu\right), \tag{88}$$

$$8\pi G\, p - \Lambda = e^{-2\nu}\left(-2\ddot{\alpha} - 3\dot{\alpha}^2 + 2\dot{\alpha}\dot{\nu}\right) + \tfrac{1}{3}e^{-2\alpha}\mathcal{M}_{kk}, \tag{89}$$

$$8\pi G\,\pi^i{}_j = e^{-2\alpha}\left(\mathcal{M}_{ij} - \tfrac{1}{3}\delta_{ij}\mathcal{M}_{kk}\right). \tag{90}$$

The Hamiltonian constraint (87) contains the lapse only through the expansion. The Lichnerowicz reconstruction of Sec. VI A therefore carries over unchanged: voids are still negative-curvature domains of the spatial scale factor.

C. Perfect fluids are allowed

The anisotropic stress (90) vanishes if

$$\begin{aligned}\Big[\partial_i\partial_j(\alpha+\nu) - \partial_i\alpha\,\partial_j\alpha + \partial_i\nu\,\partial_j\nu \\ - \partial_i\alpha\,\partial_j\nu - \partial_j\alpha\,\partial_i\nu\Big]^{\rm TF} = 0,\end{aligned} \tag{91}$$

where TF denotes the trace-free part. Unlike Theorem 1, this condition has non-FLRW solutions. Linearizing with $\alpha = \ln a + \psi$ and $\nu = \Phi$ gives $\partial_{\langle i}\partial_{j\rangle}(\psi+\Phi)=0$, i.e.

$$\Phi = -\psi = \Psi_B, \tag{92}$$

the absence of gravitational slip in general relativity. For the void of Sec. VI B the second-order correction to Eq. (92) from the quadratic terms in Eq. (91) is $\max|\Phi+\psi| = 1.5\times10^{-11}$, a fraction 3×10^{-6} of $|\psi|$. The void is thus a potential *hill* of the lapse ($\Phi>0$) and a trough of the spatial scale factor ($\psi<0$).

D. Linear dynamics

With Eq. (92) and $\delta p = 0$, the linearized trace of Eq. (89) becomes

$$\ddot{\psi} + 4H\dot{\psi} + \left(2\dot{H} + 3H^2\right)\psi = 0, \tag{93}$$

the standard equation for the Newtonian potential in a dust-plus-Λ universe [38]. Its growing solution is $\psi \propto$

$D_{\Lambda\mathrm{CDM}}/a$. Integrating Eq. (93) numerically reproduces the growth-matched factor $A(a)$ of Eq. (62) to 4×10^{-7} (Fig. 8a). The energy flux (88) becomes $8\pi G q_i = 2\partial_i(\dot\psi - H\Phi)$, which is the standard peculiar momentum, with outflow from voids. Lensing has $\Phi+\Psi = 2\Phi_N$ ($\Sigma=1$), the ISW effect has its general-relativistic amplitude, and $E_G = \Omega_m/f$.

The growth-matched closure of Sec. V C and the two-function metric thus share the same spatial scale factor $R(t,\mathbf{x}) = a(t)e^{A(t)\psi_0(\mathbf{x})}$. They differ only in the lapse, and that difference halves the lensing, halves the ISW effect and reverses the void outflow (Fig. 8b). The spatially varying scale factor is the correct description of the *spatial geometry* of voids. Their *dynamics* requires the lapse.

E. Exact examples

Two exact solutions illustrate the reach of Eq. (81). The Schwarzschild metric in isotropic coordinates,

$$e^{\nu} = \frac{1-m/2r}{1+m/2r}, \qquad e^{\alpha} = \left(1+\frac{m}{2r}\right)^2, \tag{94}$$

satisfies Eqs. (87)–(90) with $\rho=p=q=\pi=0$. McVittie's metric [82],

$$e^{\nu} = \frac{1-\mu}{1+\mu}, \qquad e^{\alpha} = a(t)(1+\mu)^2, \qquad \mu = \frac{m}{2a(t)r}, \tag{95}$$

describes a mass in an expanding universe with a perfect fluid of uniform density and inhomogeneous pressure. Formally replacing $m\to-|m|$ gives a conformal factor with a minimum at the centre, the McVittie analogue of a compensated void, though with a curvature singularity where $\mu=-1$.

F. Tidal field of a void

The electric Weyl tensor is the relativistic tidal field. In the two-function metric with $\Phi=-\psi$ it is, to linear order, $E_{ij} = a^{-2}\partial_{\langle i}\partial_{j\rangle}\Phi$. For a spherical void the radial eigenvalue is

$$E^r{}_r\big|_{\mathrm{GR}} = \frac{2}{3a^2}\left(\Phi'' - \frac{\Phi'}{r}\right) = \Omega_m H_0^2 a^{-3}\left[\delta(r) - \bar\Delta(r)\right], \tag{96}$$

where $\bar\Delta(r)$ is the mean contrast within r. The second form follows from the Poisson equation and agrees with the LTB expression (80). In the static closure, Eq. (33) with Eq. (C5) gives, to the same order,

$$E^r{}_r\big|_{\mathrm{static}} = 4\pi G\,\pi^r{}_r = -\frac{c^2}{3a^2}\left(\psi'' - \frac{\psi'}{r}\right) = \tfrac{1}{2}\,E^r{}_r\big|_{\mathrm{GR}}. \tag{97}$$

At fixed density the tidal field of a void in the conformally flat model is exactly half that of general relativity. This is the same factor that halves the lensing, since both are governed by the Weyl tensor. For the void of Sec. VI B, Eq. (96) peaks at $E^r{}_r = 0.105\,H_0^2$ near $r\simeq r_v$, and its two forms agree numerically to 10^{-4} (Fig. 7).

IX. LOCAL EXPANSION RATE, AVERAGING AND THE HUBBLE TENSION

Because voids expand faster than the background, they have been proposed as a source of local variations of the Hubble rate, and in particular of the tension between local and CMB-inferred H_0 [21]. The three cases make sharply different statements.

A. Local Hubble rate

The local Hubble rate of the comoving observers, $\mathcal{H} = \theta/3$, is

$$\mathcal{H} = \begin{cases} H & \text{(static)},\\ H+\dot\psi & \text{(growth-matched)},\\ e^{-\nu}(H+\dot\psi) \simeq H\left(1-\frac{1}{3}f\delta\right) & \text{(two-function)}. \end{cases} \tag{98}$$

In the last line we used the energy equation (36) at linear order, $\dot\delta = -\delta\theta$ in the matter frame, so that $\delta\mathcal{H}/H = -\frac{1}{3}f\delta$. In the growth-matched closure $\dot\psi = (f-1)H\psi$, so $|\delta\mathcal{H}/H| \sim |f-1|\,|\psi| \sim 10^{-5}$. In the static closure the local expansion rate is exactly uniform. Of the three, only the two-function metric reproduces the faster expansion of voids found in LTB (Sec. VII).

B. Variance and the local void

Averaged over a sphere of radius R, the rms fluctuation of the Hubble rate in linear theory is

$$\frac{\sigma_H(R)}{H} = \frac{f}{3}\,\sigma_R, \tag{99}$$

where σ_R is the rms linear density contrast in spheres of radius R. For our cosmology this gives 2.7%, 1.1%, 0.41% and 0.21% at $R=50$, 100, 200 and $300\,h^{-1}$ Mpc (Fig. 9, left). A KBC-like underdensity with $\delta=-0.3$ within $200\,h^{-1}$ Mpc would raise the local rate by 5.3%, a 13σ fluctuation by Eq. (99). This is less than the 8.3% difference between local and CMB-inferred values (73 versus $67.4\,\mathrm{km\,s^{-1}\,Mpc^{-1}}$ [70]). In the static and growth-matched closures the effect is zero or of order 10^{-5}: a spatially varying scale factor without a lapse cannot produce a local Hubble-rate excess.

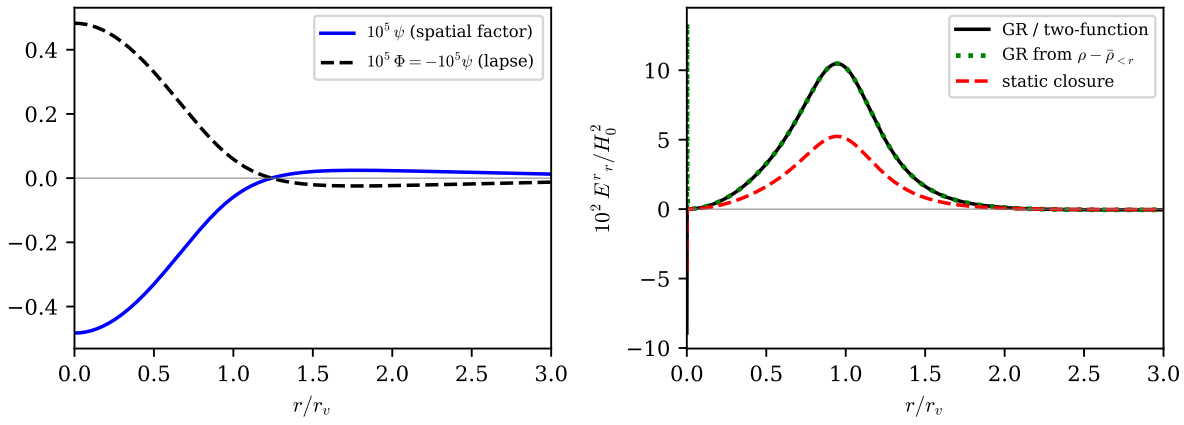


FIG. 7. Left: the spatial conformal factor ψ and the lapse $\Phi = -\psi$ of the spherical void in the two-function metric. Right: radial eigenvalue of the electric Weyl tensor in general relativity (from Φ, solid, and from $\delta - \bar{\Delta}$, dotted) and in the static closure (dashed), which is exactly half.

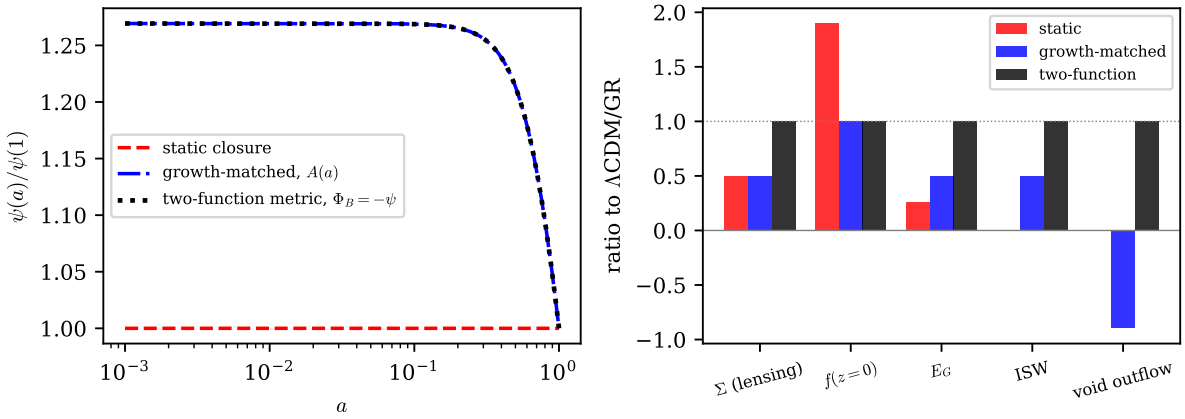


FIG. 8. (a) Time dependence of the spatial conformal factor $\psi(a)/\psi(1)$ for the static closure, the growth-matched closure and the two-function metric with $\Phi_B = -\psi$; the last two coincide. (b) Ratios of observables to ΛCDM/GR for the three cases: lensing strength Σ, growth rate f at $z = 0$, E_G, ISW amplitude and void outflow velocity.

C. Spatial averaging

For a domain $\mathcal{D}$ the Buchert equations [50] read

$$3\frac{\ddot{a}_\mathcal{D}}{a_\mathcal{D}} = -4\pi G\langle\rho\rangle_\mathcal{D} + \mathcal{Q}_\mathcal{D} + \Lambda, \tag{100}$$

$$\mathcal{Q}_\mathcal{D} = \tfrac{2}{3}\left(\langle\theta^2\rangle_\mathcal{D} - \langle\theta\rangle_\mathcal{D}^2\right) - 2\langle\sigma^2\rangle_\mathcal{D}, \tag{101}$$

where for the two-function metric $\langle\rho\rangle$ also receives a pressure-gradient contribution through the lapse. Since $\sigma = 0$ in all our cases, $\mathcal{Q}_\mathcal{D} = 6\,\mathrm{Var}_\mathcal{D}(\mathcal{H}) \geq 0$. For the two-function metric and a domain of radius $100\,h^{-1}\,$Mpc, $\mathcal{Q}_\mathcal{D}/H^2 = 6(f\sigma_R/3)^2 = 7.9\times10^{-4}$, far too small to mimic dark energy, in agreement with perturbative estimates of backreaction [49].

X. STATISTICAL ANALYSIS OF THE GALAXY DISTRIBUTION

The static closure makes the density field at any instant a deterministic and essentially linear functional of ψ, Eq. (59). Its predictions for galaxy statistics therefore differ from ΛCDM through the growth history [Eq. (60)], not through the shape of the field at fixed amplitude. To quantify this, and to test the correspondence between voids and negative curvature, we generated mock galaxy catalogues and analyzed them with the estimators used for real surveys.

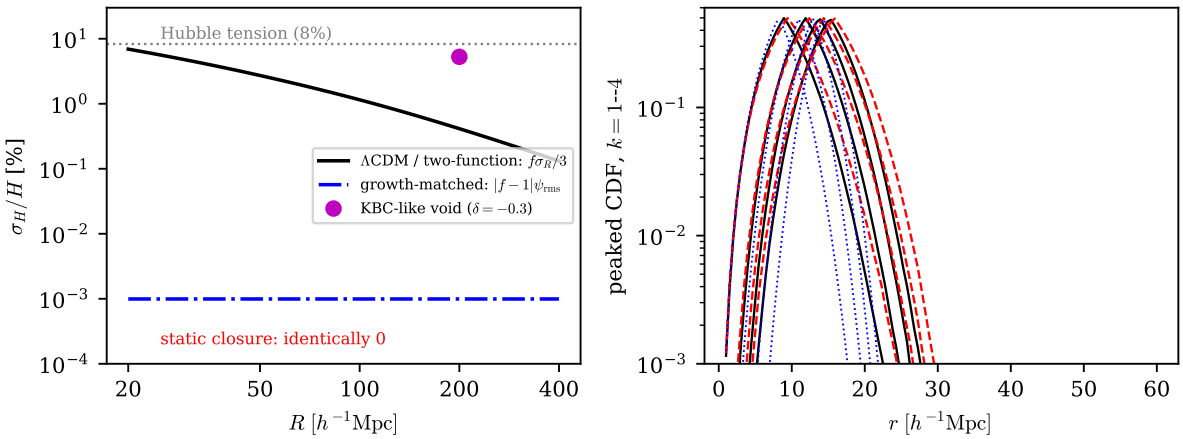


FIG. 9. Left: rms fluctuation of the local Hubble rate in spheres of radius R for ΛCDM and the two-function metric, Eq. (99), and for the growth-matched closure; the static closure has none. The point marks a KBC-like void and the dotted line the Hubble tension. Right: peaked cumulative distribution functions of the distances from random points to the k-th nearest galaxy ($k = 1$–4) for ΛCDM (solid), the static closure (dashed) and a Poisson distribution (dotted) at $z = 0$.

A. Mock catalogues

We generated a Gaussian random field on a 256^3 grid in a periodic cube of side $L = 1000\,h^{-1}\,$Mpc (cell size $3.9\,h^{-1}\,$Mpc), with the Eisenstein–Hu no-wiggle transfer function [69], $n_s = 0.965$, $h = 0.674$, $\Omega_m = 0.315$, $\Omega_b = 0.049$ and $\sigma_8 = 0.811$ [70]:

$$\delta_{\boldsymbol{k}} = W_{\boldsymbol{k}} \left[\frac{N^3 P(k)}{L^3}\right]^{1/2}, \qquad \langle |W_{\boldsymbol{k}}|^2 \rangle = N^3. \tag{102}$$

The conformal factor was obtained from the linear constraint, $\psi_{\boldsymbol{k}} = 3\Omega_m H_0^2 \delta_{\boldsymbol{k}}/(2c^2k^2)$. Evaluating the exact static-closure density (59) on the grid gave an rms difference from the linear field of 7.8×10^{-5}, compared with a cell-scale $\sigma = 1.85$. The rms conformal factor is $\psi_{\rm rms} = 2.1 \times 10^{-5}$ and the ratio of the quadratic to the linear term is 1.1×10^{-6}, confirming that the model's density field is linear in ψ.

Galaxies were drawn from a lognormal density field [71],

$$n_g(\mathbf{x}) = \bar{n} \exp\left[b\,D\,\delta_s(\mathbf{x}) - \tfrac{1}{2} b^2 D^2 \sigma_s^2\right], \tag{103}$$

where δ_s is the field smoothed with a Gaussian of radius $5\,h^{-1}\,$Mpc ($\sigma_s = 0.66$), $b = 1.5$, $\bar{n} = 3 \times 10^{-4}\,h^3\,\mathrm{Mpc}^{-3}$ (about 3×10^5 galaxies), and D is the growth factor of the model and redshift. Galaxy counts per cell were Poisson-sampled and positions placed uniformly within cells. We built six catalogues: ΛCDM and the static closure at $z = 0$, 0.5 and 1, with the same random phases and Poisson seed, so that differences are due to the growth history alone. The static closure was normalized to the same amplitude as ΛCDM at early times. Table V lists the parameters.

B. Estimators

a. Power spectrum. Galaxies were assigned to the grid with cloud-in-cell interpolation, the window was deconvolved, and the shot noise $1/\bar{n}$ was subtracted:

$$\hat{P}(k) = \frac{L^3}{N^6} \left\langle \frac{|\delta_{g,\boldsymbol{k}}|^2}{W_{\rm CIC}^2(\boldsymbol{k})} \right\rangle_{|\boldsymbol{k}|\in k} - \frac{1}{\bar{n}}. \tag{104}$$

b. Correlation function. We used the Landy–Szalay estimator [72],

$$\hat{\xi}(r) = \frac{DD(r) - 2DR(r) + RR(r)}{RR(r)}, \tag{105}$$

with normalized pair counts, computed in each of the eight octants of the box (non-periodic, with three times as many randoms as galaxies, subsampled to 3×10^4 galaxies) and averaged; errors are the scatter among octants divided by $\sqrt{8}$.

c. Counts in cells and VPF. For 10^5 random spheres of radius R we measured the count distribution $P_N(R)$, the void probability function $P_0(R)$ [73], and the Poisson-corrected moments [40, 74]

$$\bar{\xi} = \frac{\mu_2 - \bar{N}}{\bar{N}^2}, \qquad S_3 = \frac{\mu_3 - 3\mu_2 + 2\bar{N}}{\bar{N}^3 \bar{\xi}^2},$$
$$S_4 = \frac{\kappa_4 - 6\mu_3 + 11\mu_2 - 6\bar{N}}{\bar{N}^4 \bar{\xi}^3}, \tag{106}$$

where μ_n are central moments and $\kappa_4 = \mu_4 - 3\mu_2^2$.

d. Genus. The galaxy density was smoothed with a Gaussian of radius $R_G = 15\,h^{-1}\,$Mpc, and the Euler characteristic χ of excursion sets above thresholds ν_A (defined by volume fraction) was computed. The genus

density $g = -\chi/V$ was compared with the Gaussian prediction [75–77]

$$g(\nu) = \frac{1}{4\pi^2}\left(\frac{\langle k^2\rangle}{3}\right)^{3/2}(1-\nu^2)\,e^{-\nu^2/2},$$
$$\langle k^2\rangle = \frac{\int k^4 P_g(k) e^{-k^2R_G^2}dk}{\int k^2 P_g(k) e^{-k^2R_G^2}dk}. \qquad (107)$$

e. Void finder. We used a spherical-underdensity algorithm in the spirit of Refs. [10, 78]. Candidate centres are local minima of the galaxy density smoothed with a $10\,h^{-1}$ Mpc Gaussian. Around each, spheres are grown until the enclosed galaxy density first exceeds $0.2\bar{n}$ ($\Delta = -0.8$). Spheres are then ranked by radius, and a candidate is rejected if its centre lies inside an accepted void. Only voids with $R_v \geq 10\,h^{-1}$ Mpc are kept. Details are in Appendix D.

f. Theory for void abundance. For reference we computed the volume-conserving Sheth–van de Weygaert size function of matter voids [30, 31],

$$\frac{dn}{d\ln R} = \frac{f_{\ln\sigma}(\sigma)}{V(R_L)}\frac{d\ln\sigma^{-1}}{d\ln R_L},$$
$$f_{\ln\sigma} = 2\sum_{j=1}^{\infty} j\pi x^2 \sin(j\pi\mathcal{D})\,e^{-(j\pi x)^2/2}, \qquad (108)$$

with $\mathcal{D} = |\delta_v|/(\delta_c + |\delta_v|)$, $x = \mathcal{D}\sigma/|\delta_v|$, $\delta_v = -2.71$, $\delta_c = 1.686$ and $R = 1.71R_L$.

g. Tests. Void-radius distributions of the two models were compared with the two-sample Kolmogorov–Smirnov test and with a χ^2 test on binned counts.

C. Results

a. Spatial distribution. Figure 11 shows a $40\,h^{-1}$ Mpc slab of the ΛCDM catalogue at $z = 0$, with the voids that intersect it, together with slices of δ_m, ψ and the smoothed ${}^{(3)}R$. The conformal factor is a smooth, large-scale field: its power spectrum is steeper than that of δ by k^{-4}. The curvature, by Eq. (71), carries the full small-scale structure of the density. Voids sit in the troughs of ψ and, more sharply, in the negative-curvature regions.

b. Clustering. The measured power spectra and correlation functions (Fig. 12) follow the linear predictions $b^2D^2P(k)e^{-k^2R_s^2}$ on large scales and exceed them on small scales, as expected for lognormal fields. At $r \simeq 10\,h^{-1}$ Mpc we find $\hat{\xi} = 0.83 \pm 0.05$ (ΛCDM) and 1.85 ± 0.09 (static); at $r \simeq 24\,h^{-1}$ Mpc, 0.16 ± 0.01 and 0.28 ± 0.01. The ratio approaches $D^2_{\rm static}/D^2_{\Lambda\rm CDM} = 1.61$ on large scales.

c. Higher-order statistics. Counts-in-cells moments (Table V, Fig. 15) show the expected hierarchical behaviour. S_3 ranges from about 3 to 5 and increases with amplitude, as in lognormal models. The void probability function at $R = 20\,h^{-1}$ Mpc is 0.005 for ΛCDM and 0.014 for the static closure at $z = 0$, both far above the Poisson value $e^{-\bar{N}} = 4.5 \times 10^{-5}$. The genus curves (Fig. 16) are close to the Gaussian shape with the amplitude of Eq. (107) ($1.6 \times 10^{-6}\,h^3\,\mathrm{Mpc}^{-3}$), with the slight amplitude drop and asymmetry typical of mildly non-Gaussian fields. The two models are almost indistinguishable in this statistic at the same smoothing.

d. Voids. Each catalogue contains 3 000–4 000 voids with $R_v \geq 10\,h^{-1}$ Mpc, filling 14–24% of the volume (Table V). The mean radius increases with time in both models, from 19.6 to $22.8\,h^{-1}$ Mpc in ΛCDM and from 19.7 to $25.3\,h^{-1}$ Mpc in the static closure, and the largest voids reach 41 and $45\,h^{-1}$ Mpc. The cumulative void size functions (Fig. 13) separate increasingly towards $z = 0$, in the same sense as the SvdW predictions for matter voids. The absolute abundance of galaxy-defined voids differs from the matter-void theory, as is well known for sparse, biased tracers [19, 31]. Stacked galaxy profiles (Fig. 14) are empty inside $0.5R_v$, rise steeply at R_v, and show a compensating ridge of $\delta \simeq 0.1$ at 1.5–$2R_v$; this is qualitatively similar to the HSW form. The matter contrast inside voids is about -0.6 to -0.8.

e. Voids and curvature. The stacked conformal factor has a minimum of -1.8×10^{-5} near $0.5R_v$ and rises over several void radii. The stacked curvature ${}^{(3)}R$ is negative inside and changes sign near R_v (Fig. 14, right). Of the 3 488 void centres in the ΛCDM catalogue at $z = 0$, 95.3% lie where the curvature smoothed on $10\,h^{-1}$ Mpc is negative; without smoothing the fraction is 67%, limited by cell-scale noise. The Spearman correlation between void radius and the local value of ψ smoothed on 5 cells is $r_s = -0.28$ ($p = 6 \times 10^{-62}$): larger voids sit in deeper troughs of the conformal factor. Only 55% of void centres have ψ below its mean, which shows that voids trace the *curvature* of $R(t, \mathbf{x})$, not its value.

f. Local curvature at void centres. Converting the smoothed curvature to the local curvature parameter of Eq. (19) gives a direct measure of how "open" voids are (Fig. 10). Over the whole volume $\Omega_k^{\rm loc}$, smoothed on $10\,h^{-1}$ Mpc, has zero mean and rms 0.12. At void centres its mean is 0.15 (median 0.15), and 95% of the values are positive. Larger voids are more open: the Pearson correlation between R_v and $\Omega_k^{\rm loc}$ is 0.55, and the 128 voids with $R_v > 30\,h^{-1}$ Mpc have mean $\Omega_k^{\rm loc} = 0.26$, close to the value 0.27 found for the spherical HSW void of Sec. VI B.

g. Model comparison. Table VI lists the statistical tests. At $z = 0$ the void radius distributions of ΛCDM and the static closure differ with KS statistic $D = 0.24$ ($p = 1.4 \times 10^{-86}$) and $\chi^2 = 540$ for 8 degrees of freedom. At $z = 0.5$ the difference is still highly significant ($p \sim 10^{-11}$). At $z = 1$, where the growth factors differ by only 4.6%, the catalogues are statistically indistinguishable ($p_{\rm KS} = 0.16$, $p_{\chi^2} = 0.73$). Void statistics in a single $1\,h^{-3}\,\mathrm{Gpc}^3$ volume at $z \lesssim 0.5$ can therefore discriminate between the growth histories.

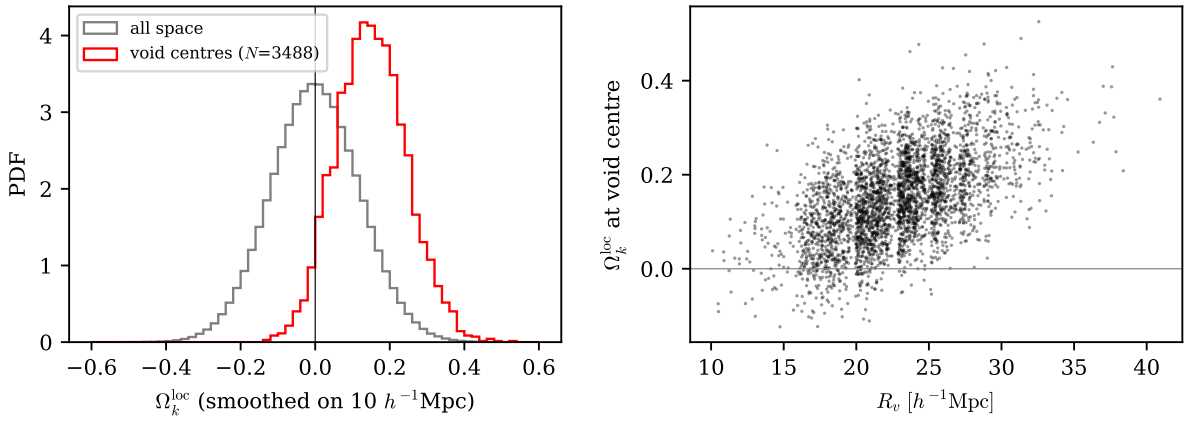


FIG. 10. Left: distribution of the local curvature parameter $\Omega_k^{\rm loc} = -{}^{(3)}Rc^2/6H_0^2$, smoothed on $10\,h^{-1}$ Mpc, over the whole volume and at void centres in the ΛCDM catalogue at $z = 0$. Right: $\Omega_k^{\rm loc}$ at void centres against void radius.

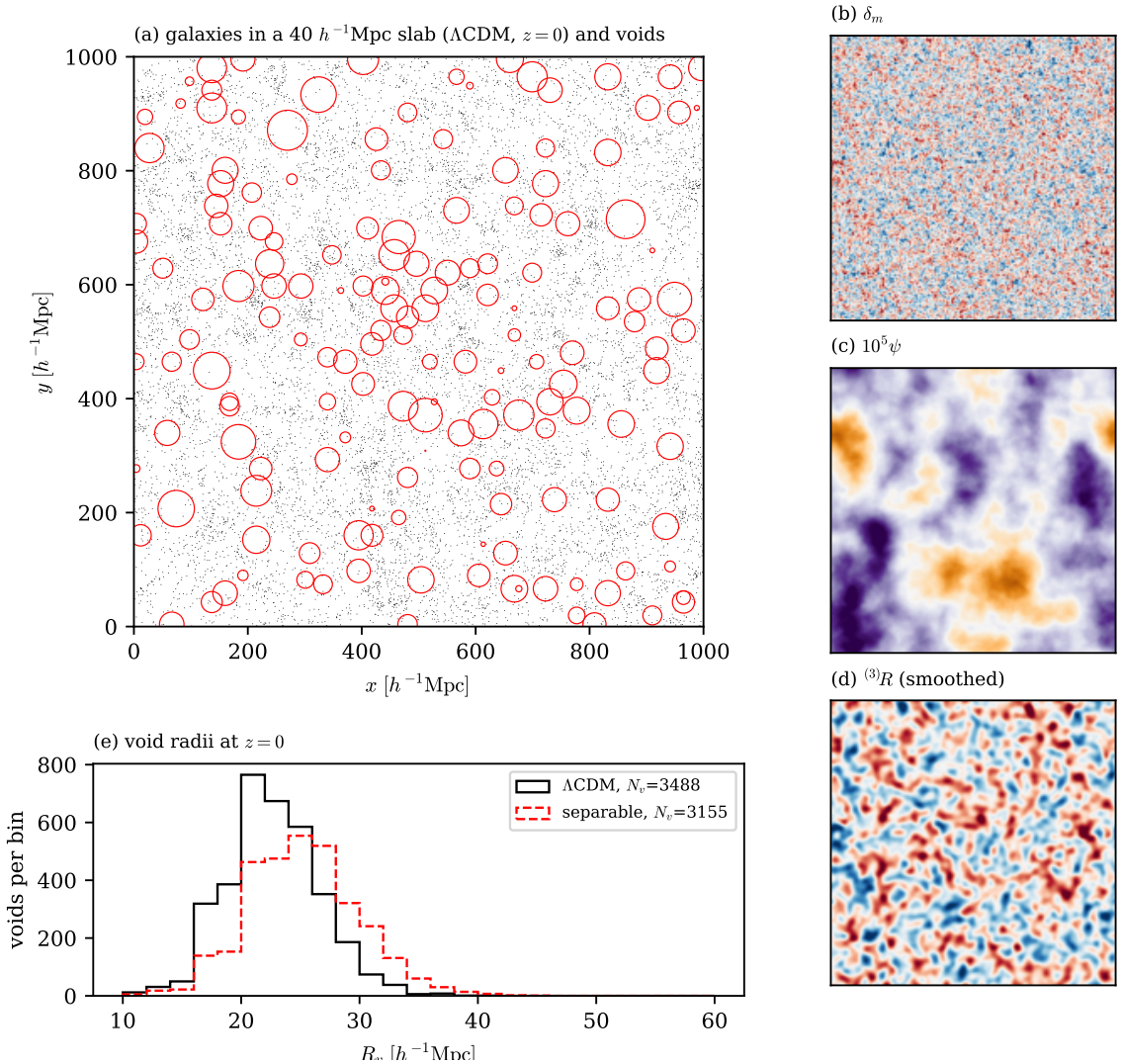


FIG. 11. (a) Galaxies in a $40\,h^{-1}$ Mpc slab of the ΛCDM catalogue at $z = 0$, with the cross-sections of voids (red circles). (b)–(d) Slices through the grid of the linear matter density, the conformal factor ψ and the spatial curvature ${}^{(3)}R$ (smoothed on $10\,h^{-1}$ Mpc). (e) Distribution of void radii in the ΛCDM and static catalogues at $z = 0$.

TABLE V. Mock catalogues and summary statistics. f_V is the volume fraction in voids. Counts-in-cells statistics are for spheres of radius 10 and $20\,h^{-1}$ Mpc.

Model	z	σ_8	$N_{\rm gal}$	N_v	$\bar{R}_v$	$R_v^{\rm max}$	f_V	$\bar{\xi}_{10}$	$S_{3,10}$	$P_0(10)$	$S_{3,20}$	$P_0(20)$
ΛCDM	0	0.811	301 043	3488	22.8	40.9	0.188	0.87	3.96	0.397	3.71	0.005
ΛCDM	0.5	0.624	300 442	3819	20.8	37.3	0.157	0.42	3.40	0.357	3.41	0.002
ΛCDM	1	0.492	300 859	4030	19.6	32.3	0.138	0.25	2.98	0.330	3.20	0.001
Static	0	1.029	300 778	3155	25.3	45.1	0.236	1.82	5.19	0.452	5.01	0.014
Static	0.5	0.686	300 555	3662	21.4	35.0	0.165	0.56	3.90	0.370	3.55	0.002
Static	1	0.515	301 123	4044	19.7	30.8	0.140	0.29	3.53	0.335	3.37	0.001

TABLE VI. Comparison of void-radius distributions between ΛCDM and the static closure in the mock catalogues.

z	$D_{\rm static}/D_{\Lambda{\rm CDM}}$	KS statistic	$p_{\rm KS}$	χ^2/dof	p_{χ^2}
0	1.269	0.243	1.4×10^{-86}	540/8	1.7×10^{-111}
0.5	1.101	0.080	6.6×10^{-11}	66.8/6	1.8×10^{-12}
1	1.046	0.025	0.16	2.8/5	0.73

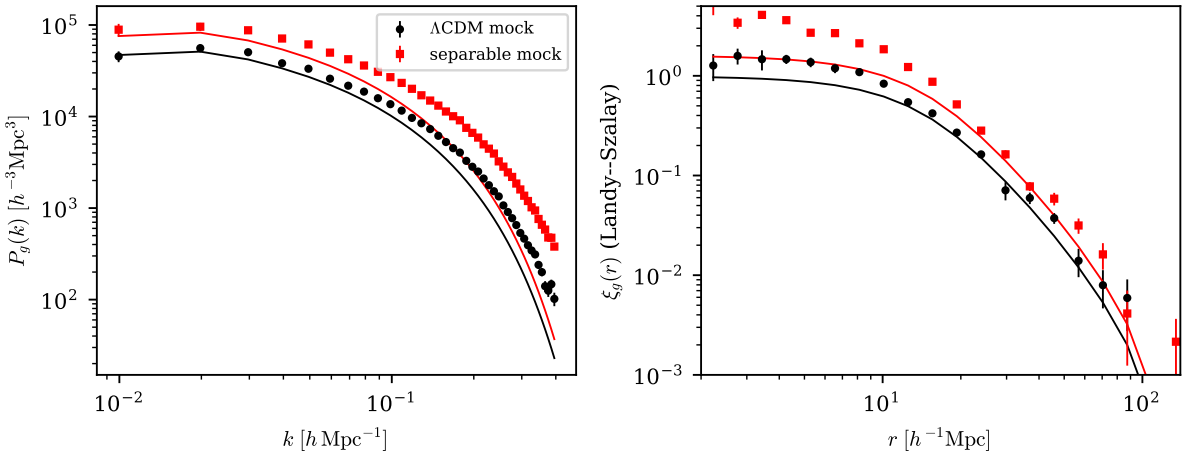


FIG. 12. Galaxy power spectrum (left) and Landy–Szalay correlation function (right) of the ΛCDM and static catalogues at $z = 0$. Lines are the linear predictions $b^2D^2P(k)e^{-k^2R_s^2}$ and their Fourier transforms.

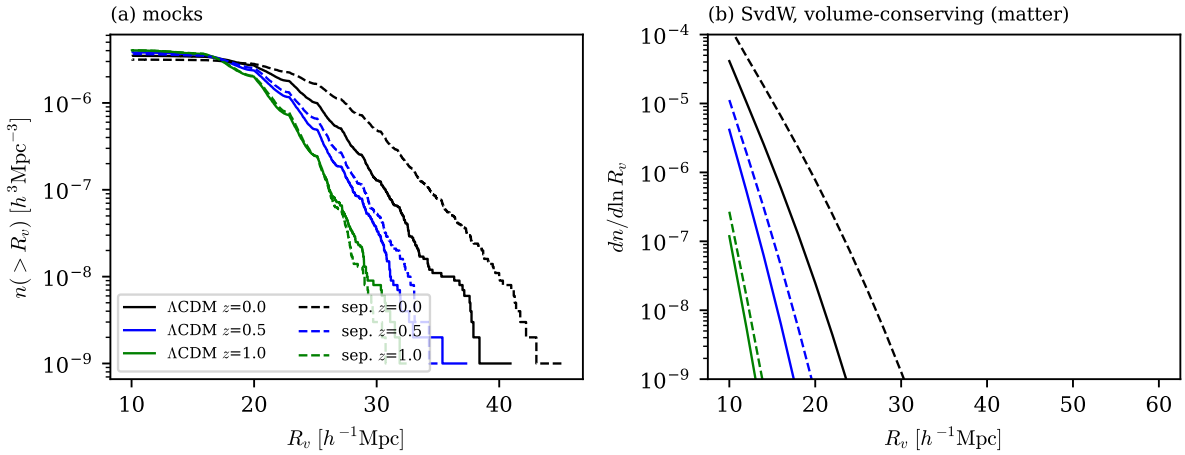


FIG. 13. (a) Cumulative void size functions of the six catalogues. (b) Volume-conserving SvdW size functions for matter voids with the corresponding amplitudes.

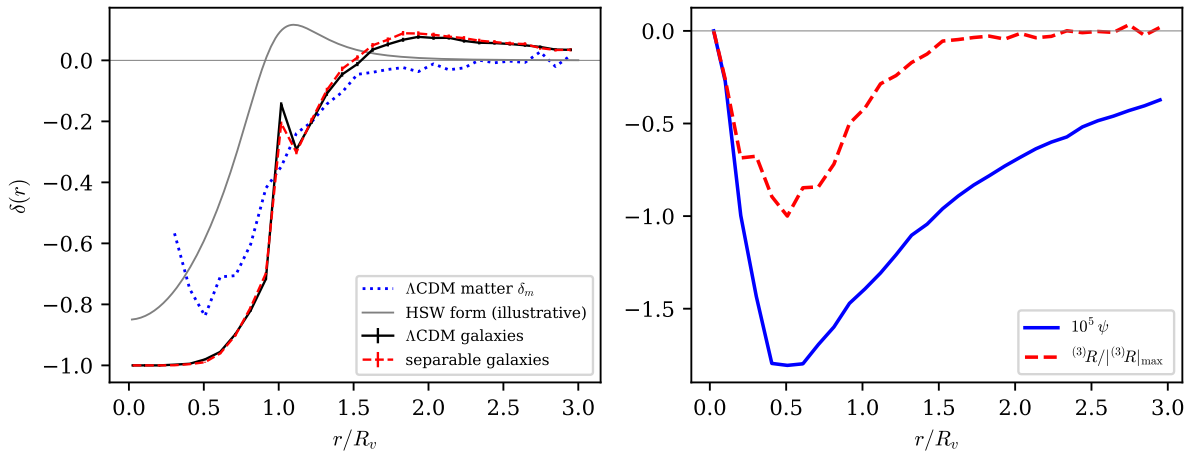


FIG. 14. Left: stacked void profiles in galaxies (both models, $z = 0$), in matter (ΛCDM) and the HSW form for comparison. Right: stacked conformal factor ψ and normalized spatial curvature ${}^{(3)}R$ around voids in the ΛCDM catalogue.

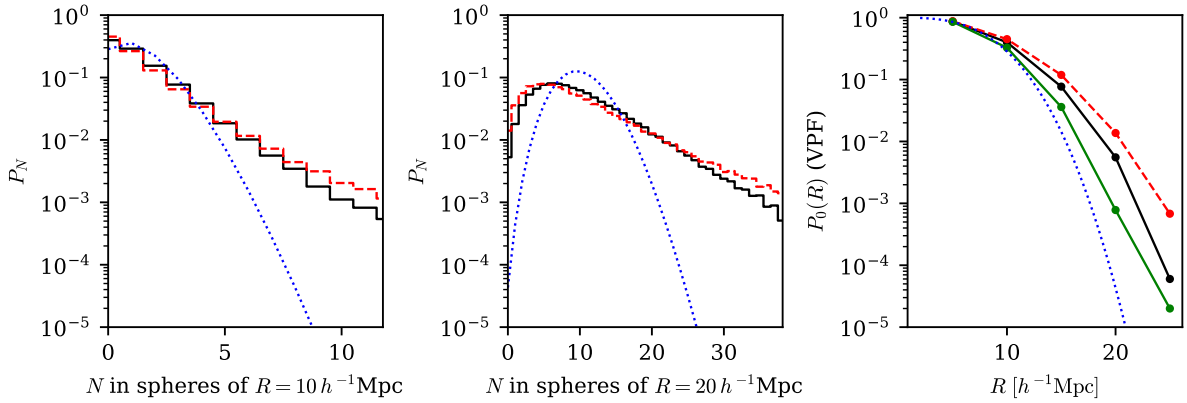


FIG. 15. Counts-in-cells distributions for spheres of radius 10 and $20\,h^{-1}$ Mpc (solid: ΛCDM, dashed: static closure, dotted: Poisson) and void probability function (right; green: ΛCDM at $z = 1$).

D. Higher-order statistics: absence of gravitational skewness

The exact static-closure density (59), expanded to second order in ψ, is

$$\delta = \frac{-2c^2}{3\Omega_m H_0^2}\, a\left[\nabla^2\psi\,(1-2\psi) + \tfrac{1}{2}(\nabla\psi)^2\right] + O(\psi^3). \quad (109)$$

The second-order terms are suppressed relative to the first by $|\psi| \sim 10^{-5}$. If the primordial ψ is Gaussian, the static-closure matter field is therefore Gaussian to one part in 10^5, and its reduced skewness vanishes:

$$S_3^{\rm static} \equiv \frac{\langle\delta^3\rangle}{\langle\delta^2\rangle^2} = O(\psi) \sim 10^{-5}. \quad (110)$$

Gravitational instability instead generates non-Gaussianity at second order through the kernel [40]

$$F_2(\boldsymbol{k}_1,\boldsymbol{k}_2) = \frac{5}{7} + \frac{1}{2}\frac{\boldsymbol{k}_1\cdot\boldsymbol{k}_2}{k_1 k_2}\left(\frac{k_1}{k_2}+\frac{k_2}{k_1}\right) + \frac{2}{7}\frac{(\boldsymbol{k}_1\cdot\boldsymbol{k}_2)^2}{k_1^2 k_2^2}, \quad (111)$$

which for top-hat smoothing gives

$$S_3^{\rm PT} = \frac{34}{7} + \frac{d\ln\sigma_R^2}{d\ln R} = \frac{34}{7} - (n_{\rm eff}+3). \quad (112)$$

For our spectrum $n_{\rm eff} = -1.53$ and -1.20 at $R = 10$ and $20\,h^{-1}$ Mpc, so $S_3^{\rm PT} = 3.39$ and 3.06. Measured galaxy skewness in large surveys is hierarchical with values of this order [96, 97]. Such skewness cannot arise in the static closure without primordial non-Gaussianity of ψ. (Our lognormal mocks impose $S_3 \simeq 3 + \sigma^2$ by construction in both cases, so Table V does not test this prediction.) This is a further, independent discriminant: a

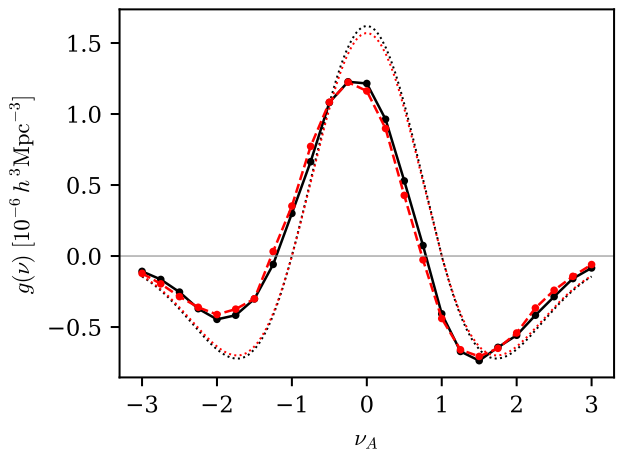


FIG. 16. Genus density of the galaxy field smoothed on $15\,h^{-1}$ Mpc for the two models at $z = 0$, with the Gaussian predictions of Eq. (107) (dotted).

spatially varying scale factor without gravitational dynamics imprints the initial statistics of ψ directly on the galaxy distribution.

E. Void bias and void shapes

On large scales voids are biased tracers of the matter field [17]. We estimated the void bias from the ratio of the void–galaxy to the galaxy–galaxy correlation function at $40 \le r \le 85\,h^{-1}$ Mpc, $b_v = b\,\xi_{vg}/\xi_{gg}$, in three bins of void radius. Small voids ($10 \le R_v < 20\,h^{-1}$ Mpc) have positive bias, $b_v \approx 6.1$ (ΛCDM) and 7.7 (static), because they are embedded in overdense regions ("void-in-cloud"). Intermediate voids (20–30 h^{-1} Mpc) have $b_v \approx 1.0$ and 1.8. The largest voids ($\ge 30\,h^{-1}$ Mpc) have negative bias, $b_v \approx -6.7$ and -4.4 (Fig. 17). The sign change with radius reproduces the behaviour found in simulations and surveys [17, 30]. The bias values are indicative only, since they rest on small correlation amplitudes and, for the largest voids, on 128 and 486 objects.

Void shapes were measured from the inertia tensor of galaxies in the shell $R_v < r < 1.3R_v$ around voids with $R_v > 15\,h^{-1}$ Mpc. The mean axis ratios are $\langle b/a\rangle = 0.81$ and $\langle c/a\rangle = 0.64$ for ΛCDM, and 0.80 and 0.63 for the static closure, comparable to the asphericity of voids in Gaussian fields [26, 98]. The shape distributions of the two models are almost identical. Shapes are set mainly by the geometry of the initial field and depend only weakly on the growth amplitude.

F. Void centres as minima of the curvature field

In the static closure ${}^{(3)}R \propto \delta$ [Eq. (71)], so the minima of the smoothed density field are the minima of the spatial curvature, and void centres are a subset of them. For a Gaussian field smoothed with $W = e^{-k^2R_G^2/2}$, the number density of minima of any height is [94]

$$n_{\rm min} = \frac{29 - 6\sqrt{6}}{5^{3/2}\,8\pi^2}\,R_*^{-3} \simeq \frac{0.0162}{R_*^3}, \qquad R_* = \sqrt{\frac{3\sigma_1^2}{\sigma_2^2}}, \tag{113}$$

with spectral moments

$$\sigma_j^2 = \frac{1}{2\pi^2}\int k^{2+2j}P(k)\,W^2(kR_G)\,dk, \qquad \gamma = \frac{\sigma_1^2}{\sigma_0\sigma_2}. \tag{114}$$

Counting local minima of the smoothed linear field on the 256^3 grid gives 7 093, 2 324 and 1 057 minima for $R_G = 10$, 15 and $20\,h^{-1}$ Mpc, against Eq. (113) predictions of 7 318, 2 386 and 1 075. The agreement is 97–98%, and the residual deficit is due to grid discreteness. The galaxy field smoothed on $10\,h^{-1}$ Mpc yields 3 519 candidate centres with the coarser selection of Appendix D, from which the void finder retains 3 488. Void abundance in the model is therefore controlled by the peak statistics of the curvature field, with R_* ranging from 13 to $25\,h^{-1}$ Mpc and $\gamma = 0.72$–0.75.

G. Nearest-neighbour distributions

The k-nearest-neighbour cumulative distribution functions (kNN-CDFs) [95], i.e. the distributions of distances from random points to the k-th nearest galaxy, are sensitive to all connected correlation functions and especially to voids. For a Poisson process,

$$\mathrm{CDF}_k(r) = P\!\left(k,\ \tfrac{4}{3}\pi\bar{n}r^3\right), \tag{115}$$

where P is the regularized lower incomplete gamma function, and $1 - \mathrm{CDF}_1(r)$ is the void probability function. We measured $\mathrm{CDF}_{1\text{–}4}$ from 2×10^5 random points (Fig. 9, right). The median distances for $k = 1$–4 are 8.95, 11.88, 13.76 and $15.21\,h^{-1}$ Mpc for ΛCDM and 9.46, 12.44, 14.35 and $15.80\,h^{-1}$ Mpc for the static closure, against 8.44, 10.92, 12.90 and $14.39\,h^{-1}$ Mpc for Poisson. Clustering shifts all CDFs to larger distances, and the static closure, with 27% more growth, shifts them further.

H. Redshift-space distortions

The three cases differ most clearly in their velocity fields. In linear theory, a galaxy at real-space position $\mathbf{x}$ appears along the line of sight $\hat{z}$ at

$$s_z = x_z + f_{\rm eff}\,\Psi_z(\mathbf{x}), \qquad \Psi_{\boldsymbol{k}} = \frac{i\boldsymbol{k}}{k^2}\,\delta_{\boldsymbol{k}}, \tag{116}$$

where $\boldsymbol{\Psi}$ is the linear displacement field and $f_{\rm eff}$ the effective growth rate of the velocities. For ΛCDM (and the two-function metric) $f_{\rm eff} = f = 0.527$ at $z = 0$. For the static closure $f_{\rm eff} = 0$, since there is no flow relative

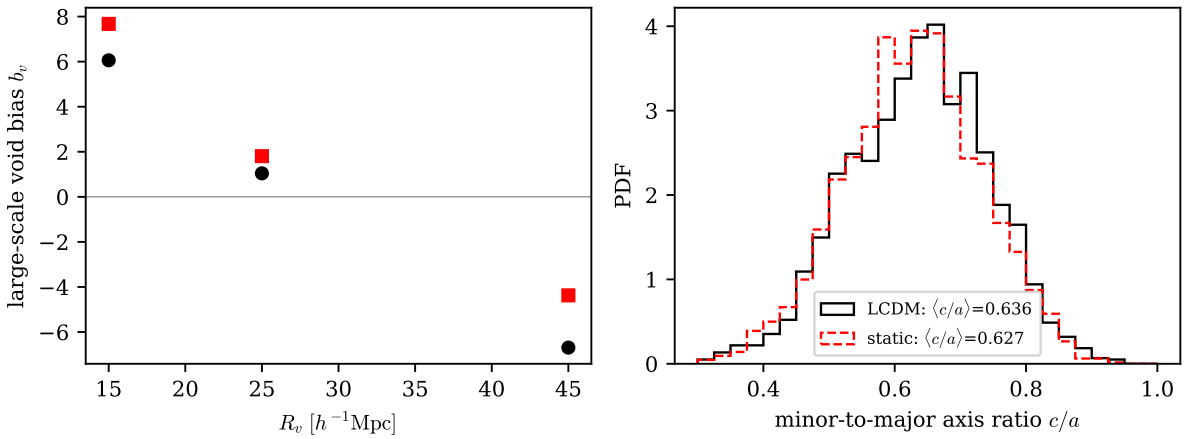


FIG. 17. Left: large-scale void bias as a function of void radius for ΛCDM (circles) and the static closure (squares) at $z = 0$. Right: distribution of the minor-to-major axis ratio of voids from the galaxy inertia tensor in the shell $R_v < r < 1.3R_v$.

to u^a. For the growth-matched closure, Eq. (63) gives $f_{\rm eff} = f - 1 = -0.473$. We applied Eq. (116) to the ΛCDM catalogue at $z = 0$, using the displacement of the smoothed field, and measured two statistics.

a. Power-spectrum multipoles. The Legendre multipoles of the redshift-space power spectrum [83],

$$P_\ell(k) = \frac{2\ell+1}{2}\int_{-1}^{1} P(k,\mu)\,\mathcal{L}_\ell(\mu)\,d\mu, \tag{117}$$

with $\mu = \hat{k}\cdot\hat{z}$, were estimated on the grid; modes with $k_z > 0$ were weighted twice to account for the real-FFT half-space. In the Kaiser limit [84],

$$\frac{P_2}{P_0} = \frac{\frac{4}{3}\beta + \frac{4}{7}\beta^2}{1 + \frac{2}{3}\beta + \frac{1}{5}\beta^2}, \qquad \beta = \frac{f_{\rm eff}}{b}. \tag{118}$$

b. Void–galaxy cross-correlation. Voids were identified in real space ($15 < R_v < 40\,h^{-1}$ Mpc; 3 418 voids), and the multipoles $\xi_0(s)$ and $\xi_2(s)$ of the void–galaxy correlation were measured in redshift space in units of s/R_v. The linear model of Refs. [85, 86] predicts

$$\xi_2(s) = \frac{2\beta}{3}\left[\xi^r(s) - \bar{\xi}^r(s)\right], \tag{119}$$

$$\bar{\xi}^r(s) = \frac{3}{s^3}\int_0^s \xi^r(s')s'^2 ds', \tag{120}$$

where ξ^r is the real-space void–galaxy profile.

c. Results. Table VII and Fig. 18 summarize the measurements.

- *ΛCDM:* $P_2/P_0 = 0.395\pm0.018$ for $k < 0.1\,h\,\mathrm{Mpc}^{-1}$, against the Kaiser value 0.428. The small deficit is the familiar nonlinear (Fingers-of-God-like) suppression from the lognormal field.
- *Static closure:* $P_2/P_0 = 0.007 \pm 0.015$, consistent with zero.
- *Growth-matched closure:* $P_2/P_0 = -0.395 \pm 0.016$, a negative quadrupole.

The void–galaxy quadrupole averaged over $1.2 < s/R_v < 2.2$ shows the same pattern: $+0.034 \pm 0.006$, $+0.001 \pm 0.003$ and -0.039 ± 0.004 respectively, against linear predictions of $+0.060$, 0 and -0.054. Every redshift survey has measured a positive large-scale quadrupole [79, 80], and void–galaxy quadrupoles are consistent with outflow [18, 86]. Both closures of the $g_{00} = -1$ model are therefore excluded by the *sign* or the *existence* of redshift-space distortions, independently of amplitude.

I. Comparison with observed void catalogues

Public void catalogues from SDSS and BOSS [12–14] contain voids of effective radius $\sim$ 10–100 h^{-1} Mpc with stacked profiles well described by Eq. (73) [17]. Their abundances, shapes and redshift-space distortions agree with ΛCDM simulations [13, 18, 19]. Redshift-space void–galaxy correlations show coherent outflows consistent with linear theory [18]. In the static closure these outflows are absent (Sec. V C); in the growth-matched closure the energy flux points inward at late times [Eq. (63)]. Section X H shows that this produces a vanishing or negative void–galaxy quadrupole. Both closures are therefore in tension with void dynamics, independently of the growth-rate and E_G arguments of Sec. V. A quantitative fit to survey data, including survey geometry, redshift-space distortions and selection, is beyond the scope of this paper; the estimators of this section apply unchanged.

TABLE VII. Redshift-space statistics of the $z = 0$ mock for the three velocity fields. P_2/P_0 is averaged over $k < 0.1\,h\,\mathrm{Mpc}^{-1}$; $\langle\xi_2\rangle$ over $1.2 < s/R_v < 2.2$.

Case	$f_{\rm eff}$	P_2/P_0	Kaiser	$\langle\xi_2\rangle$	Linear
ΛCDM	0.527	0.395(18)	0.428	0.034(6)	0.060
Static	0	0.007(15)	0	0.001(3)	0
Growth-matched	−0.473	−0.395(16)	−0.449	−0.039(4)	−0.054

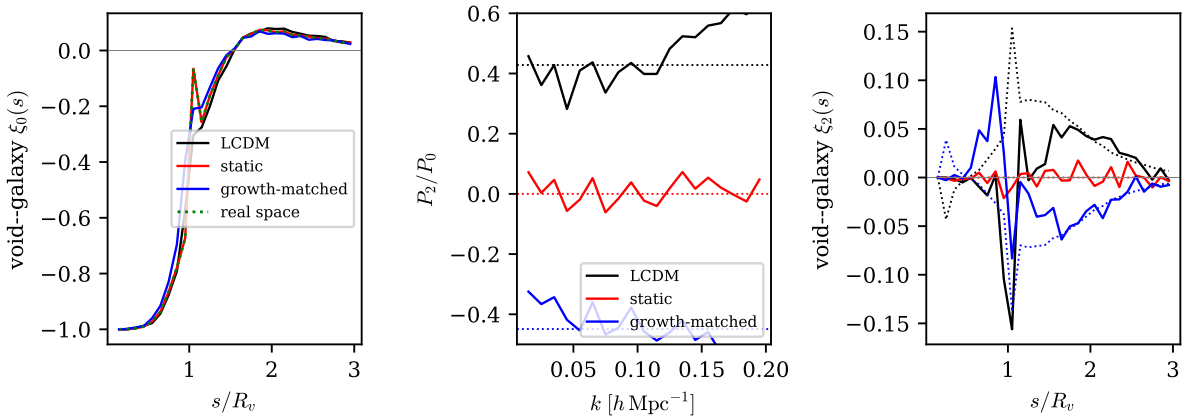


FIG. 18. Redshift-space statistics of the ΛCDM mock with the velocity fields of the three cases. Left: void–galaxy monopole in real and redshift space. Centre: power-spectrum quadrupole-to-monopole ratio with the Kaiser predictions (dotted). Right: void–galaxy quadrupole with the linear predictions of Eq. (120) (dotted).

XI. CONFRONTATION WITH GROWTH AND LENSING DATA

We now fit the three cases to published measurements of the growth rate and of the lensing-to-velocity ratio.

A. Data

For $f\sigma_8(z)$ we use eight measurements: 6dFGS at $z = 0.067$ [87], the SDSS main galaxy sample at $z = 0.15$ [88], the three BOSS DR12 consensus bins at $z = 0.38$, 0.51 and 0.61 [79], and the eBOSS LRG, ELG and quasar samples at $z = 0.70$, 0.85 and 1.48 [80]. For E_G we use five measurements at $z = 0.32$ and 0.57 [64, 89–91]. The values are listed in Table VIII. We use diagonal errors. The BOSS bins are correlated at the $\sim 30\%$ level and several E_G measurements share data, so the χ^2 values below are indicative; the differences between models are large enough that this does not affect the conclusions.

B. Models

All models use $\Omega_m = 0.315$ and have one free amplitude, $\sigma_8 \equiv \sigma_8(z = 0)$:

$$\Lambda\mathrm{CDM}: \quad f\sigma_8 = f(z)\,\sigma_8\,\frac{D(z)}{D(0)}, \quad E_G = \frac{\Omega_m}{f(z)}, \tag{121}$$

$$\text{static}: \quad f\sigma_8 = \frac{\sigma_8}{1+z}, \quad E_G = \frac{\Omega_m}{2}, \tag{122}$$

$$\text{growth-matched}: \quad f\sigma_8 \text{ as } \Lambda\mathrm{CDM}, \quad E_G = \frac{\Omega_m}{2f(z)}. \tag{123}$$

For the static closure we take the generous view that the growth rate $f = 1$ would be measured. Since this closure has no peculiar velocities, a literal prediction would be $f\sigma_8 = 0$, which is excluded at very high significance. We also fit the phenomenological growth index [92], $f = \Omega_m(a)^\gamma$, with σ_8 and γ free and $E_G = \Omega_m/f$.

C. Results

Table IX and Fig. 19 give the results.

- *ΛCDM:* $\chi^2 = 17.8$ for 12 degrees of freedom, with $\sigma_8 = 0.808$.

TABLE VIII. Data used in the fit (diagonal errors).

Sample	z	Value	Ref.
6dFGS	0.067	$f\sigma_8 = 0.423 \pm 0.055$	[87]
SDSS MGS	0.15	0.53 ± 0.16	[88]
BOSS DR12	0.38	0.497 ± 0.045	[79]
BOSS DR12	0.51	0.459 ± 0.038	[79]
BOSS DR12	0.61	0.436 ± 0.034	[79]
eBOSS LRG	0.70	0.473 ± 0.041	[80]
eBOSS ELG	0.85	0.315 ± 0.095	[80]
eBOSS QSO	1.48	0.462 ± 0.045	[80]
SDSS LRG	0.32	$E_G = 0.39 \pm 0.06$	[64]
RCSLenS/CFHTLenS	0.32	0.48 ± 0.10	[89]
RCSLenS/CFHTLenS	0.57	0.30 ± 0.07	[89]
Planck×CMASS	0.57	0.243 ± 0.060	[90]
CFHTLenS×CMASS	0.57	0.42 ± 0.056	[91]

TABLE IX. Best fits to the data of Table VIII (13 points).

Model	σ_8	$\chi^2_{f\sigma_8}$	$\chi^2_{E_G}$	χ^2	$\Delta\chi^2$	ΔAIC
ΛCDM	0.808	7.3	10.5	17.8	0	0
Static	0.683	36.4	53.6	90.0	72.2	72.2
Growth-matched	0.808	7.3	31.5	38.8	21.0	21.0
γ free ($\gamma = 0.48$)	0.791	8.5	8.6	17.1	-0.7	1.3

- *Static closure:* $\Delta\chi^2 = +72.2$; its best fit, $\sigma_8 = 0.68$, tries to compromise between $f = 1$ at all redshifts and the low $E_G = \Omega_m/2$.
- *Growth-matched closure:* it fits $f\sigma_8$ by construction but has $\Delta\chi^2 = +21.0$ from E_G alone.
- *Growth index:* $\gamma = 0.48^{+0.08}_{-0.08}$ ($\Delta\chi^2 = 1$ interval 0.40–0.56), consistent with the general-relativistic value $\gamma \simeq 0.55$. The value $\gamma = 0$ ($f = 1$) is excluded.

In terms of the Akaike information criterion [93], AIC $= \chi^2 + 2k$, the static and growth-matched closures are disfavoured by ΔAIC $= 72$ and 21.

D. Cosmic-shear power spectrum

Because the model lenses with $\Sigma = 1/2$ [Eq. (58)], the convergence power spectrum in the Limber approximation [58],

$$C_\ell^{\kappa\kappa} = \int_0^{\chi_s} \frac{d\chi}{\chi^2}\, W^2(\chi)\, \Sigma^2\, P\!\left(\frac{\ell + 1/2}{\chi}, z\right), \qquad (124)$$

$$W(\chi) = \frac{3\Omega_m H_0^2}{2c^2} \frac{\chi(\chi_s - \chi)}{\chi_s\, a}, \qquad (125)$$

is reduced by $\Sigma^2 = 1/4$ at fixed matter power. For sources at $z_s = 1$ (Fig. 20), the growth-matched closure gives exactly 1/4 of the ΛCDM spectrum. The static closure, with its larger late-time growth, gives 0.32 of it at $\ell = 100$. A survey interpreting such data with general relativity would infer $S_8 \equiv \sigma_8(\Omega_m/0.3)^{1/2}$ lower by a factor of two than the clustering amplitude. The observed lensing amplitudes are lower than the CMB-inferred value by only of order 10%, the so-called S_8 tension. The model's factor of two is therefore excluded by cosmic-shear surveys as well.

XII. DISCUSSION

A. What the spatially varying scale factor explains

The metric (1) provides an exact, covariant and economical description of a cosmic void. In the static closure:

1. every void corresponds to a solution of the Lichnerowicz equation (70);
2. the void is a domain of negative spatial curvature whose local Ω_k equals $-\Omega_m(a)\delta$;
3. the conformal factor needed is tiny ($|\psi| \sim 10^{-6}$–10^{-4}) and smooth, so a nearly homogeneous $R(t, \mathbf{x})$ produces a strongly inhomogeneous galaxy distribution;
4. the tidal field around the void is the electric Weyl tensor $4\pi G\pi_{ab}$.

In the mocks, voids identified purely from galaxy positions coincide with negative-curvature domains for 95% of their centres. In this geometric sense, large voids are regions where the spatial scale factor R is locally "more open", not regions where it is larger.

B. What it does not explain

Three properties of the model conflict with data when it is treated as a closed cosmological model.

1. *No lapse.* With $g_{00} = -1$ there is no Newtonian potential in the time–time component, so comoving matter feels no gravitational acceleration ($\Phi_B = 0$), and lensing is halved ($\Sigma = 1/2$). The E_G measurements disfavor this at ~ 3–4σ.
2. *Growth.* A static spatial factor gives $D \propto a$ with $f = 1$ even during acceleration, which is excluded by redshift-space-distortion measurements of $f\sigma_8$ [79, 80]. Reproducing ΛCDM growth requires a time-dependent ψ, which brings an energy flux with the wrong sign relative to observed void outflows.
3. *Effective fluid.* By Theorem 1, any inhomogeneity requires anisotropic stress. In the static closure the inhomogeneous component has $w = -1/3$ and no peculiar velocity, unlike clustering dust.

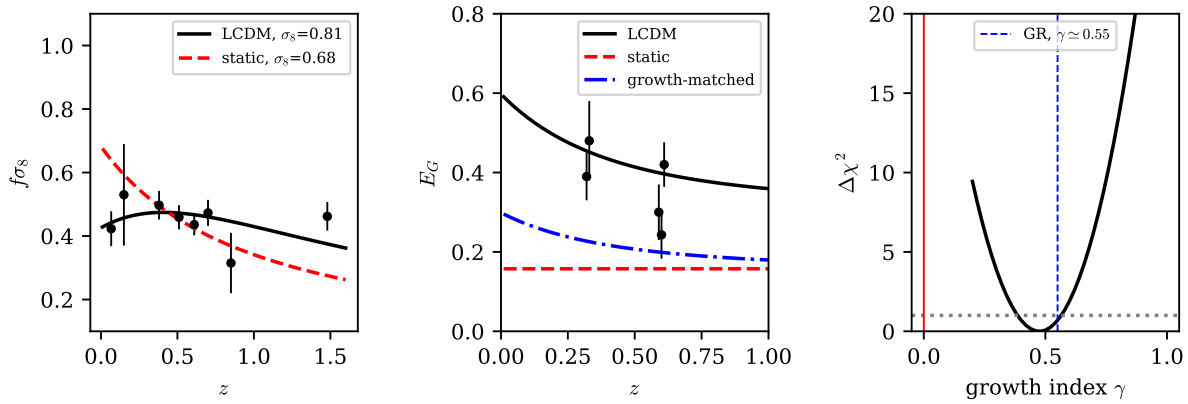


FIG. 19. Left: $f\sigma_8$ data with the best-fitting ΛCDM and static-closure curves. Centre: E_G data with the predictions of ΛCDM, the static closure and the growth-matched closure. Right: profile $\Delta\chi^2$ for the growth index γ; the static closure corresponds to $\gamma = 0$.

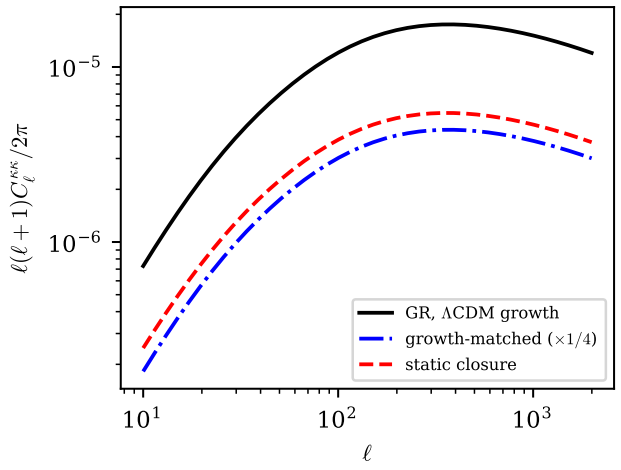


FIG. 20. Linear convergence power spectrum for sources at $z_s = 1$ in general relativity with ΛCDM growth, and in the growth-matched and static closures ($\Sigma = 1/2$).

The model does not alter the rarity of the largest voids (Table III): since the density is linear in ψ, Gaussian ψ gives the same void statistics as Gaussian δ at fixed amplitude. Only non-Gaussian initial conditions for ψ, or a different growth history, could change them.

Table X summarizes the predictions of the three realizations.

C. Possible physical interpretations of the effective fluid

The stresses required by Eqs. (26)–(27) could be interpreted in several ways. (a) *Backreaction and coarse-graining*: averaging an inhomogeneous dust universe produces effective curvature and stress terms [49–51]. For our congruence the kinematical backreaction is $\mathcal{Q}_D = \frac{2}{3}(\langle\theta^2\rangle_D - \langle\theta\rangle_D^2) - 2\langle\sigma^2\rangle_D = 6\,\mathrm{Var}_D(\dot{\alpha}) \geq 0$, which acts with the sign of acceleration. It vanishes in the static closure and is of order $(H\psi)^2 \sim 10^{-10}H^2$ in the growth-matched one, so it is negligible. (b) *Modified gravity*, in which a gravitational slip is generic [62]; the extreme slip of Eq. (57) is, however, disfavored. (c) *A dark sector with anisotropic stress*, such as a scalar field with gradient energy: $T_{ij} \supset \partial_i\varphi\partial_j\varphi$ contains a term of the form $\partial_i\alpha\,\partial_j\alpha$ in Eq. (27), but no single minimally coupled field reproduces the $\partial_i\partial_j\alpha$ term. (d) *A coordinate artefact*: the metric is the Newtonian gauge with Φ set to zero, and adding back the lapse $g_{00} = -(1+2\Phi)$ restores standard general relativity with dust. Interpretation (d) leads to the two-function metric of Sec. VIII, in which voids are still negative-curvature domains of R but are now also potential hills of the lapse N, and the effective fluid becomes ordinary pressureless matter.

D. Relation to exact inhomogeneous models

The LTB models are spherically symmetric dust solutions with $g_{rr} = R'^2/(1+2E)$ and areal radius $R(t,r)$ [41–43]. They are not conformally flat in general, and each shell evolves as an independent FLRW universe with its own curvature, so voids are naturally open regions. Our model is conformally flat with an unperturbed lapse. It coincides with LTB only in the FLRW limit, but shares the identification of voids with locally open geometry. The Stephani models [45] are conformally flat perfect fluids with a spatially varying pressure and a non-trivial lapse; Theorem 1 shows that removing the lapse forces them back to FLRW. Szekeres models [44] have no symmetry but are again dust with a non-trivial spatial metric. Among these, the conformally flat ansatz is the most restrictive and the only one that requires imperfect sources. Section VII makes the comparison with LTB

TABLE X. Summary of predictions for the three realizations of a spatially varying scale factor, compared with ΛCDM/GR at fixed density field. "Ref." gives the section where each is derived or tested.

Observable	Static closure	Growth-matched closure	Two-function metric	Ref.
Perfect-fluid source possible	no	no	yes	III, VIII
Growth rate $f(z=0)$	1	0.53	0.53	V C
Lensing strength Σ	1/2	1/2	1	IV B
Tidal field E_{ab}	$\frac{1}{2}$ GR	$\frac{1}{2}$ GR	GR	VIII F
E_G at $z=0.32$	0.16	0.23	0.45	XI
ISW amplitude	0	$\frac{1}{2}$ GR	GR	IV
Redshift-space quadrupole	0	negative	positive (Kaiser)	X H
Void outflow	none	inflow	outflow	V C
Local Hubble excess in voids	0	$\sim 10^{-5}$	$-\frac{1}{3}f\delta$	IX
Matter skewness S_3 (Gaussian ψ)	$\sim 10^{-5}$	$\sim 10^{-5}$	$34/7-(n_{\rm eff}+3)$	X D
Cosmic-shear power	0.32 (at $\ell=100$)	1/4	1	XI D
$\Delta\chi^2$ vs ΛCDM ($f\sigma_8$+E_G)	+72	+21	0	XI
Voids as negative-curvature domains	yes	yes	yes	VI

quantitative.

E. Other void-based proposals

Large voids have been invoked to explain several anomalies: the apparent acceleration in giant-void LTB models [48, 49], the local Hubble-rate excess [21], and the CMB Cold Spot through the ISW effect of the Eridanus supervoid [22]. The present framework places all three in a common geometric language, since each concerns the local curvature and expansion of $R(t,\mathbf{x})$. It also shows that the static and growth-matched closures cannot help with any of them. The static closure has no local Hubble excess and no ISW effect, and the growth-matched closure has an ISW signal of half the general-relativistic amplitude, which makes the Cold Spot harder to explain. Only the two-function metric reproduces the standard predictions. The size of these effects then depends on the rarity of the voids, which Table III shows to be extreme in Gaussian ΛCDM statistics.

F. Observational tests

The model makes sharp predictions that differ from ΛCDM at fixed density field:

1. stacked void and cluster lensing at half the general-relativistic amplitude;
2. $E_G = \Omega_m/2$ (static) or $\Omega_m/(2f)$ (growth-matched);
3. no ISW signal (static) or half the general-relativistic ISW (growth-matched), for example in stacked supervoid ISW measurements [81];
4. no redshift-space distortions around voids (static), or inward-pointing energy flux (growth-matched);
5. void abundance at $z=0$ enhanced by the factor implied by $D_{\rm static}/D_{\Lambda\rm CDM}=1.27$.

Sections X H and XI confront items 2 and 4 with mocks and with published data; both closures fail, while the two-function metric passes by construction.

G. Extensions

Several generalizations are natural. (i) An *anisotropic* scale factor, $g_{ij}=R_{ij}(t,\mathbf{x})$, would allow sheared expansion, as in LTB and Szekeres models, at the cost of losing conformal flatness and the Lichnerowicz structure. (ii) In the two-function metric, nonlinear voids could be modelled with McVittie-type ansätze, Eq. (95), with a smooth negative-mass profile in place of the point mass, or by matching to LTB interiors. (iii) A light-cone treatment, integrating Eq. (43) and the Sachs equation (50) through realizations of ψ, would give distance–redshift relations and void lensing maps directly in the model. (iv) Applying the void finder, the curvature reconstruction (Lichnerowicz equation) and the redshift-space estimators of Secs. X and X H to DESI and Euclid void catalogues would turn the geometric picture into a measurement of the spatial curvature field around voids.

XIII. CONCLUSIONS

We have worked out the Einstein equations for the FLRW line element with a scale factor $R(t,x,y,z)$ depending on space as well as time. The curvature is given in closed form. The comoving observers are geodesic, shear-free and irrotational. The source is an imperfect fluid whose energy flux is the gradient of the local Hubble rate and whose anisotropic stress is the trace-free spatial curvature, and the Weyl tensor is purely electric and equal to $4\pi G$ times that stress. Perfect fluids force the metric back to FLRW.

Voids appear as domains of negative spatial curvature, reconstructed exactly from any density profile by a Lichnerowicz equation. They need conformal factors of only 10^{-6}–10^{-4}, and in mock catalogues they coincide with negative-curvature regions for 95% of their centres. The static version of the model grows structure as $D = a$, and is distinguished from ΛCDM by the void size function at $z \lesssim 0.5$ with overwhelming significance in a gigaparsec volume. All versions halve gravitational lensing at fixed density. Growth-rate, lensing-to-velocity and void-outflow data therefore disfavor the model as a closed cosmology.

Its value is twofold. It gives an exact geometric language in which voids are regions where the spatial scale factor is locally open. It also shows, through an explicit and exactly solvable example, that the time–time component of the metric is indispensable for the dynamics of voids. An exact LTB void confirms that the static model is a linear approximation, and redshift-space statistics together with a fit to thirteen growth and lensing measurements disfavor both closures ($\Delta\chi^2 = 72$ and 21). Restoring the lapse, $-N^2dt^2 + R^2d\mathbf{x}^2$, removes every one of these difficulties: perfect fluids are allowed, the slip vanishes, and ΛCDM dynamics is recovered, while voids remain negative-curvature domains of R. Applying the estimators presented here to survey void catalogues within this two-function framework, including nonlinear stages via exact solutions such as McVittie-type and LTB-type geometries, is the natural next step.

ACKNOWLEDGMENTS

Financial support for this work was provided by SpARC, Gyansarovar, Mount Abu, Rajasthan, India. The author acknowledges the use of Claude, an artificial-intelligence model developed by Anthropic.

DATA AVAILABILITY

The scripts that generate every number, table and figure in this paper are available from the author on request. They comprise the symbolic derivations of the curvature for both metrics, the background, closure, Lichnerowicz and LTB numerics, the mock catalogues and their real- and redshift-space statistics, the void-finder robustness tests, and the likelihood fit. The measurements used in the fit are listed in Table VIII.

Appendix A: Notation

Table XI collects the principal symbols.

TABLE XI. Principal symbols.

Symbol	Meaning
$R(t,\mathbf{x})$	spacetime-dependent scale factor
u^a	comoving four-velocity
α	conformal exponent, $e^\alpha = R/(1+kr^2/4)$
$\theta,\ A_a$	expansion, acceleration
$a(t)$	background scale factor
$\sigma_{ab},\ \omega_{ab}$	shear, vorticity
ψ	excess conformal factor, $\alpha = \ln a + \psi$
$\rho,\ p$	effective density, isotropic pressure
$\nu,\ N = e^\nu$	lapse exponent and lapse
$q_a,\ \pi_{ab}$	energy flux, anisotropic stress
${}^{(3)}R$	Ricci scalar of $t =$ const slices
$E_{ab},\ H_{ab}$	electric, magnetic Weyl tensors
$\Omega_k^{\rm loc}$	local curvature parameter
$\Phi_B,\ \Psi_B$	Bardeen potentials
$w = e^{\psi/2}$	Lichnerowicz variable
$\Sigma,\ \mu$	lensing and growth modifications
$D,\ f$	growth function and rate
E_G	lensing-to-velocity ratio
$A(a)$	growth-matched amplitude
$\Delta_a,\ \mathcal{Z}_a$	covariant gradient variables
$\delta_c,\ r_v,\ r_s$	HSW profile parameters
$R_v,\ N_v,\ f_V$	void radius, number, volume fraction
$\bar\xi,\ S_3,\ S_4$	counts-in-cells moments
$P_0(R)$	void probability function
$b,\ b_v$	galaxy and void bias
$\beta = f_{\rm eff}/b$	redshift-space distortion parameter
$\mathcal{H}$	local Hubble rate $\theta/3$
$\mathcal{Q}_\mathcal{D}$	kinematical backreaction

Appendix B: Connection and curvature components

From Eqs. (6)–(8), the Riemann tensor $R^a{}_{bcd} = \partial_c\Gamma^a_{bd} - \partial_d\Gamma^a_{bc} + \Gamma^a_{ce}\Gamma^e_{bd} - \Gamma^a_{de}\Gamma^e_{bc}$ has the independent components

$$R^0{}_{i0j} = e^{2\alpha}\left(\ddot\alpha + \dot\alpha^2\right)\delta_{ij}, \tag{B1}$$

$$R^0{}_{ijk} = e^{2\alpha}\left(\delta_{ik}\partial_j\dot\alpha - \delta_{ij}\partial_k\dot\alpha\right), \tag{B2}$$

$$R^i{}_{jkl} = {}^{(3)}R^i{}_{jkl} + e^{2\alpha}\dot\alpha^2\left(\delta^i_k\delta_{jl} - \delta^i_l\delta_{jk}\right), \tag{B3}$$

where the purely spatial curvature of $e^{2\alpha}\delta_{ij}$ is

$$ {}^{(3)}R_{ijkl} = e^{2\alpha}\big(\delta_{il}\,\mathcal{A}_{jk} + \delta_{jk}\,\mathcal{A}_{il} - \delta_{ik}\,\mathcal{A}_{jl} - \delta_{jl}\,\mathcal{A}_{ik}\big),$$
$$\mathcal{A}_{ij} = \partial_i\partial_j\alpha - \partial_i\alpha\,\partial_j\alpha + \tfrac{1}{2}\delta_{ij}(\nabla\alpha)^2. \tag{B4}$$

Contracting gives Eqs. (9)–(11). Equation (B2) is the Codazzi relation with extrinsic curvature $K_{ij} = \dot\alpha\, e^{2\alpha}\delta_{ij}$, and Eq. (B3) is the Gauss relation. For FLRW one has $\mathcal{A}_{ij} \propto \delta_{ij}$ and $R^0{}_{ijk} = 0$.

The Kretschmann scalar follows from the decomposition into Weyl and Ricci parts,

$$R_{abcd}R^{abcd} = C_{abcd}C^{abcd} + 2R_{ab}R^{ab} - \tfrac{1}{3}R^2, \tag{B5}$$

with $C_{abcd}C^{abcd}$ from Eq. (34) and $R_{ab} = 8\pi G\left(T_{ab} - \frac{1}{2}Tg_{ab}\right) + \Lambda g_{ab}$ evaluated from Eqs. (24)–(27). It is finite wherever α is smooth: the voids constructed here contain no curvature singularities.

Appendix C: Spherical reduction

For $\alpha = \alpha(t, r)$, with $' \equiv \partial_r$,

$$\nabla^2\alpha = \alpha'' + \frac{2}{r}\alpha', \qquad (\nabla\alpha)^2 = \alpha'^2, \tag{C1}$$

$$8\pi G\rho + \Lambda = 3\dot\alpha^2 - e^{-2\alpha}\left(2\alpha'' + \frac{4}{r}\alpha' + \alpha'^2\right), \tag{C2}$$

$$8\pi G\, q_r = 2\dot\alpha', \tag{C3}$$

$$\begin{aligned} 8\pi G\, p - \Lambda &= -\left(2\ddot\alpha + 3\dot\alpha^2\right) \\ &\quad + \tfrac{1}{3}e^{-2\alpha}\left(2\alpha'' + \frac{4}{r}\alpha' + \alpha'^2\right), \end{aligned} \tag{C4}$$

$$\begin{aligned} 8\pi G\, \pi^r{}_r &= -16\pi G\, \pi^\theta{}_\theta \\ &= \tfrac{2}{3}e^{-2\alpha}\left(\alpha'^2 - \alpha'' + \frac{\alpha'}{r}\right). \end{aligned} \tag{C5}$$

The electric Weyl tensor has eigenvalues $E^r{}_r = -2E^\theta{}_\theta = 4\pi G\pi^r{}_r$. The Misner–Sharp-like mass within areal radius $\mathcal{R} = re^\alpha$ is

$$\begin{aligned} M(t,r) &= \frac{\mathcal{R}}{2G}\left(1 - \nabla_a\mathcal{R}\nabla^a\mathcal{R}\right) \\ &= \frac{\mathcal{R}}{2G}\left[\mathcal{R}^2\dot\alpha^2 - r\alpha'(2 + r\alpha')\right], \end{aligned} \tag{C6}$$

using $\nabla_a\mathcal{R}\nabla^a\mathcal{R} = -(\partial_t\mathcal{R})^2 + e^{-2\alpha}(\partial_r\mathcal{R})^2$ with $\partial_t\mathcal{R} = \mathcal{R}\dot\alpha$ and $\partial_r\mathcal{R} = e^\alpha(1 + r\alpha')$. A void, with $\alpha' > 0$ inside, has a mass deficit relative to the background term $\mathcal{R}^3\dot\alpha^2/2G$.

Appendix D: Numerical methods

a. Symbolic verification. The Christoffel symbols, Riemann, Ricci and Einstein tensors of Eq. (3) were computed symbolically for arbitrary $\alpha(t, x, y, z)$, reproducing Eqs. (9)–(15) and (12) exactly. Equation (33) was checked by evaluating C_{i0j0} and π_{ij} at a test point for a non-separable α.

b. Background and closures. The ΛCDM growth function was computed from $D(a) = \frac{5}{2}\Omega_m E(a)\int_0^a [a'E(a')]^{-3}da'$ with $E^2 = \Omega_m a^{-3} + \Omega_\Lambda$. Equation (61) was integrated in $\ln a$ from $a = 10^{-3}$ with a fifth-order Runge–Kutta method and relative tolerance 10^{-8}.

c. Lichnerowicz equation. Equation (72) was integrated outward to $r = 5r_v$ with relative tolerance 10^{-11}, using the regular expansion $w''(0) = -K\delta(0)/3$ at the origin. Doubling the resolution changes $\psi(0)$ by less than 10^{-4} in relative terms. The lensing convergence uses the Born approximation along straight lines through the void.

d. Mocks and void finder. Fields were generated by fast Fourier transform. Void candidates are local minima of the galaxy density on a 128^3 grid smoothed with a $10\,h^{-1}\,$Mpc Gaussian. For each candidate the 600 nearest galaxies are found with a periodic k-d tree; the void radius is the largest neighbour distance r_k at which $(k-1)/(\frac{4}{3}\pi r_k^3\bar n) \le 0.2$. Overlapping candidates are removed in order of decreasing radius. The genus uses the 26-connectivity Euler number of the thresholded 128^3 field. The Landy–Szalay pair counts use k-d tree neighbour counting.

Appendix E: The two-function metric in detail

For Eq. (81) the nonvanishing Christoffel symbols are

$$\Gamma^0_{00} = \dot\nu, \qquad \Gamma^0_{0i} = \partial_i\nu, \qquad \Gamma^0_{ij} = \dot\alpha\, e^{2\alpha-2\nu}\delta_{ij}, \tag{E1}$$

$$\Gamma^i_{00} = e^{2\nu-2\alpha}\partial_i\nu, \qquad \Gamma^i_{0j} = \dot\alpha\,\delta^i_j, \tag{E2}$$

with Γ^i_{jk} as in Eq. (8). The Einstein tensor is given by Eqs. (82)–(85). We verified these expressions, including all off-diagonal spatial components, with a symbolic computation for arbitrary $\alpha(t, \mathbf{x})$ and $\nu(t, \mathbf{x})$. The trace of $\mathcal{M}_{ij}$ is

$$\mathcal{M}_{kk} = 2\nabla^2\alpha + (\nabla\alpha)^2 + 2\nabla^2\nu + 2(\nabla\nu)^2 + 2\nabla\alpha\cdot\nabla\nu. \tag{E3}$$

a. Spherical symmetry. For $\alpha(t, r)$ and $\nu(t, r)$ the condition (91) for vanishing anisotropic stress becomes the ordinary differential equation

$$\nu'' + \alpha'' - \alpha'^2 + \nu'^2 - 2\alpha'\nu' - \frac{\alpha' + \nu'}{r} = 0. \tag{E4}$$

Its homogeneous linear solutions $\nu + \alpha = c_0 + c_2r^2$ correspond to a constant shift of the lapse and to spatial curvature. The isotropic Schwarzschild metric (94) satisfies Eq. (E4) exactly. For the void of Sec. VI B we solved Eq. (E4) perturbatively, $\nu = -\psi + \eta$, with the decaying boundary condition $\eta' \to 0$. The quadratic source $-2\psi'^2$ gives $|\eta| \le 1.5 \times 10^{-11}$.

b. Linearized equations. With $\alpha = \ln a + \psi$ and $\nu = \Phi$,

$$8\pi G\,\delta\rho = 6H(\dot\psi - H\Phi) - \frac{2c^2}{a^2}\nabla^2\psi, \tag{E5}$$

$$8\pi G\, q_i = 2c\,\partial_i(\dot\psi - H\Phi), \tag{E6}$$

$$\begin{aligned} 8\pi G\,\delta p &= -2\ddot\psi - 6H\dot\psi + 2H\dot\Phi + 2(2\dot H + 3H^2)\Phi \\ &\quad + \frac{2c^2}{3a^2}\nabla^2(\psi + \Phi), \end{aligned} \tag{E7}$$

$$8\pi G\,\pi^i{}_j = -\frac{c^2}{a^2}\left(\partial_i\partial_j - \tfrac{1}{3}\delta_{ij}\nabla^2\right)(\psi + \Phi). \tag{E8}$$

With $\Psi_B = -\psi$ and $\Phi_B = \Phi$ these are the Newtonian-gauge equations of Refs. [38, 39]. Setting $\Phi = 0$ recovers Eqs. (51)–(54).

Appendix F: Robustness of the void statistics

To test whether the discrimination between ΛCDM and the static closure (Table VI) depends on analysis choices, we repeated the $z = 0$ void analysis while varying one choice at a time:

- the void density threshold, $\Delta = -0.7$ and -0.9;
- the smoothing scale used to select candidate centres, 5 and $15\,h^{-1}\,$Mpc;
- the galaxy bias, $b = 1.2$ and 2.0;
- the number density, $\bar{n} = 10^{-4}$ and $10^{-3}\,h^3\,\mathrm{Mpc}^{-3}$, with minimum radii of 15 and $7\,h^{-1}\,$Mpc;
- the Poisson sampling seed.

Table XII lists the results. Void numbers and sizes change with the definition, as expected. In every case, however, the static closure produces larger voids that fill more volume, and the Kolmogorov–Smirnov test separates the two models with $\log_{10} p$ between -34 and -115. Changing the Poisson seed alters $\log_{10} p$ by about 6, which indicates the sampling scatter of this statistic.

a. Lichnerowicz integration. The central conformal factor of the void in Sec. VI B is independent of the integration tolerance (10^{-8} versus 10^{-11}) and of the sampling (2001 versus 5001 points) to better than 10^{-9} in relative terms. It depends on the outer boundary through the normalization $\psi(r_{\max}) = 0$: $\psi(0) = -4.87$, -4.83 and -4.75×10^{-6} for $r_{\max} = 4$, 5 and $8\,r_v$. The HSW profile with the parameters used is not exactly compensated (its mean contrast within r_v is not cancelled by the ridge), so ψ has a weak $1/r$ tail. The quoted value therefore carries a $\sim 2\%$ boundary uncertainty, which affects none of the conclusions.

Appendix G: Consistency checks in the FLRW limit

For $\alpha = \ln a(t) - \ln(1 + \frac{1}{4}kr^2)$, with $\phi \equiv 1 + \frac{1}{4}kr^2$,

$$\partial_i\alpha = -\frac{kx_i}{2\phi}, \qquad (\nabla\alpha)^2 = \frac{k^2r^2}{4\phi^2}, \tag{G1}$$

$$\partial_i\partial_j\alpha = -\frac{k\delta_{ij}}{2\phi} + \frac{k^2x_ix_j}{4\phi^2}, \qquad \nabla^2\alpha = -\frac{3k}{2\phi} + \frac{k^2r^2}{4\phi^2}. \tag{G2}$$

Hence $\partial_i\partial_j\alpha - \partial_i\alpha\,\partial_j\alpha = -k\delta_{ij}/(2\phi)$ is pure trace, so $\pi_{ij} = 0$ [Eq. (27)], and

$$2\nabla^2\alpha + (\nabla\alpha)^2 = -\frac{3k}{\phi} + \frac{3k^2r^2}{4\phi^2} = -\frac{3k}{\phi^2}, \tag{G3}$$

so that $e^{-2\alpha}[2\nabla^2\alpha + (\nabla\alpha)^2] = -3k/a^2$. Equations (24)–(26) then reduce to the Friedmann equations,

$$8\pi G\rho + \Lambda = 3H^2 + \frac{3k}{a^2}, \qquad 8\pi G p - \Lambda = -2\frac{\ddot{a}}{a} - H^2 - \frac{k}{a^2}, \tag{G4}$$

with ${}^{(3)}R = 6k/a^2$ from Eq. (17), $q_i = 0$ and $E_{ab} = 0$, as required. The redshift formula (43) reduces to $1 + z = a_o/a_e$, because $\exp(-\int\nabla\alpha\cdot d\mathbf{x}) = \phi(\mathbf{x}_o)/\phi(\mathbf{x}_e)$ cancels the spatial factors in $R_{\rm eff} = a/\phi$. The Lichnerowicz equation (70) with uniform $\delta\rho$ is solved by $w = \phi^{-1/2}$ (up to the factor $a^{-1/2}$) with $k = \frac{8\pi G}{3c^2}a^2\delta\rho$: a uniform density excess is equivalent to positive spatial curvature, which is the separate-universe statement. In the two-function metric, $\nu = \nu(t)$ is a time reparametrization and the same checks apply with $dt \to e^{\nu}dt$.

Appendix H: Series and asymptotic solutions of the Lichnerowicz equation

Near the centre of a spherical void, with $\delta(r) = \delta_0 + \frac{1}{2}\delta_2 r^2 + O(r^4)$ and $K \equiv 3\Omega_m H_0^2/(4c^2a)$, Eq. (72) has the regular expansion

$$w(r) = w_0 - \frac{K\delta_0 w_0^5}{6}\,r^2 + \left(\frac{K^2\delta_0^2 w_0^9}{24} - \frac{K\delta_2 w_0^5}{40}\right)r^4 + O(r^6), \tag{H1}$$

so that $\psi = 2\ln w$ has curvature $\psi''(0) = -\frac{2}{3}K\delta_0 w_0^4 > 0$ in a void. For $r \to \infty$, where $\delta \to 0$, the solution approaches the harmonic form

$$w(r) \to w_\infty\left(1 + \frac{\mu}{r}\right), \qquad \mu = \frac{K}{w_\infty}\int_0^\infty \delta\, w^5\, r^2\, dr, \tag{H2}$$

which is the Lichnerowicz analogue of the exterior Schwarzschild solution: a void with net mass deficit has $\mu < 0$ and a $1/r$ tail in ψ. For an exactly compensated profile $\mu = 0$ at linear order and ψ decays faster. This explains the weak dependence of $\psi(0)$ on the outer boundary noted in Appendix F. Existence and uniqueness of positive solutions for $\delta \geq -1$ follow from the sub- and super-solution method for semilinear elliptic equations of Lichnerowicz type [66].

Appendix I: Analytic lensing of a top-hat void

For a uniform underdense sphere of comoving radius r_v and contrast $\delta_v < 0$, compensated by a thin shell, the projected contrast is

$$\int \delta\, d\ell = 2\delta_v\sqrt{r_v^2 - R^2}\,\Theta(r_v - R), \tag{I1}$$

and the convergence in general relativity follows from the Born approximation as

$$\kappa_{\rm GR}(R) = \frac{3\Omega_m H_0^2}{c^2}\,\frac{\chi_l(\chi_s - \chi_l)}{\chi_s\,a_l}\,\delta_v\sqrt{r_v^2 - R^2}, \qquad R < r_v. \tag{I2}$$

The mean convergence within R and the tangential shear $\gamma_t = \bar{\kappa} - \kappa$ follow by elementary integration:

$$\begin{aligned}\bar{\kappa}_{\rm GR}(R) &= \frac{2}{R^2}\int_0^R \kappa_{\rm GR}(R')R'dR' \\ &= \kappa_0\,\frac{2r_v^3 - 2(r_v^2 - R^2)^{3/2}}{3r_vR^2},\end{aligned} \tag{I3}$$

with $\kappa_0 = \kappa_{\rm GR}(0)$. In the $R(t,\mathbf{x})$ model every expression is multiplied by $1/2$. For $\delta_v = -0.85$, $r_v = 30\,h^{-1}\,$Mpc,

TABLE XII. Void statistics at $z = 0$ under variations of the analysis. N_v: number of voids; $\bar{R}_v$: mean radius in $h^{-1}\,\mathrm{Mpc}$; f_V: volume fraction; KS: two-sample Kolmogorov–Smirnov statistic between the two models and $\log_{10}$ of its p value.

	ΛCDM			Static closure				
Variation	N_v	$\bar{R}_v$	f_V	N_v	$\bar{R}_v$	f_V	KS D	$\log_{10} p$
Fiducial	3488	22.8	0.188	3155	25.3	0.236	0.243	−85.9
$\Delta = -0.7$	3459	25.2	0.254	3108	28.0	0.317	0.238	−81.2
$\Delta = -0.9$	3486	19.9	0.129	3179	22.2	0.164	0.220	−70.2
Candidate smoothing $5\,h^{-1}\,\mathrm{Mpc}$	6997	20.5	0.275	6090	22.4	0.318	0.195	−107.6
Candidate smoothing $15\,h^{-1}\,\mathrm{Mpc}$	1501	24.1	0.101	1468	27.5	0.145	0.250	−40.5
$b = 1.2$	3736	21.1	0.161	3501	22.9	0.192	0.188	−55.6
$b = 2.0$	3156	25.9	0.253	2810	29.5	0.336	0.280	−102.2
$\bar{n} = 10^{-4}$	3357	27.4	0.315	3077	29.2	0.348	0.156	−33.6
$\bar{n} = 10^{-3}$	3125	19.5	0.110	2934	22.9	0.166	0.293	−114.6
Poisson seed 2	3486	22.8	0.189	3204	25.3	0.240	0.233	−79.5

$z_l = 0.3$ and $z_s = 1$, Eq. (I2) gives $\kappa_0 = -1.8 \times 10^{-3}$, about twice the numerical value for the smoother, partly self-compensated HSW profile of Table II.

Appendix J: Statistical conventions

a. Errors. Correlation-function errors are $\sigma_\xi = \mathrm{std}(\xi_i)/\sqrt{N_\mathrm{sub}}$ over $N_\mathrm{sub} = 8$ independent octants. Power-spectrum errors are $\sigma_P = \mathrm{std}(P_{\boldsymbol{k}})/\sqrt{N_{\boldsymbol{k}}}$ over the modes in each shell. Void-size-function comparisons use Poisson errors on binned counts.

b. Tests. The two-sample Kolmogorov–Smirnov statistic is $D = \sup_R |F_1(R) - F_2(R)|$, where F_i are the empirical cumulative distributions of void radii. Its p value follows from the asymptotic distribution with effective sample size $n_1 n_2/(n_1 + n_2)$. The binned test uses

$$\chi^2 = \sum_\mathrm{bins} \frac{(N_1 - N_2)^2}{N_1 + N_2}, \tag{J1}$$

with the number of non-empty bins as degrees of freedom.

c. Model comparison. For the fits of Sec. XI we use $\chi^2 = \sum_i [(d_i - m_i)/\sigma_i]^2$ and the Akaike information criterion $\mathrm{AIC} = \chi^2_\mathrm{min} + 2k$ for k free parameters [93]. A difference $\Delta\mathrm{AIC} > 10$ is conventionally regarded as decisive.

[1] S. A. Gregory and L. A. Thompson, Astrophys. J. **222**, 784 (1978).
[2] R. P. Kirshner, A. Oemler, P. L. Schechter, and S. A. Shectman, Astrophys. J. Lett. **248**, L57 (1981).
[3] R. P. Kirshner, A. Oemler, P. L. Schechter, and S. A. Shectman, Astrophys. J. **314**, 493 (1987).
[4] V. de Lapparent, M. J. Geller, and J. P. Huchra, Astrophys. J. Lett. **302**, L1 (1986).
[5] M. J. Geller and J. P. Huchra, Science **246**, 897 (1989).
[6] M. Colless *et al.*, Mon. Not. R. Astron. Soc. **328**, 1039 (2001).
[7] D. G. York *et al.*, Astron. J. **120**, 1579 (2000).
[8] J. R. Gott III, M. Jurić, D. Schlegel, F. Hoyle, M. Vogeley, M. Tegmark, N. Bahcall, and J. Brinkmann, Astrophys. J. **624**, 463 (2005).
[9] H. El-Ad and T. Piran, Astrophys. J. **491**, 421 (1997).
[10] F. Hoyle and M. S. Vogeley, Astrophys. J. **566**, 641 (2002).
[11] F. Hoyle and M. S. Vogeley, Astrophys. J. **607**, 751 (2004).
[12] D. C. Pan, M. S. Vogeley, F. Hoyle, Y.-Y. Choi, and C. Park, Mon. Not. R. Astron. Soc. **421**, 926 (2012).
[13] P. M. Sutter, G. Lavaux, B. D. Wandelt, and D. H. Weinberg, Astrophys. J. **761**, 44 (2012).
[14] Q. Mao *et al.*, Astrophys. J. **835**, 161 (2017).
[15] G. Lavaux and B. D. Wandelt, Mon. Not. R. Astron. Soc. **403**, 1392 (2010).
[16] G. Lavaux and B. D. Wandelt, Astrophys. J. **754**, 109 (2012).
[17] N. Hamaus, P. M. Sutter, and B. D. Wandelt, Phys. Rev. Lett. **112**, 251302 (2014).
[18] N. Hamaus, A. Pisani, P. M. Sutter, G. Lavaux, S. Escoffier, B. D. Wandelt, and J. Weller, Phys. Rev. Lett. **117**, 091302 (2016).
[19] A. Pisani *et al.*, Bull. Am. Astron. Soc. **51**, 40 (2019), arXiv:1903.05161.
[20] R. van de Weygaert and E. Platen, Int. J. Mod. Phys. Conf. Ser. **1**, 41 (2011).
[21] R. C. Keenan, A. J. Barger, and L. L. Cowie, Astrophys. J. **775**, 62 (2013).
[22] I. Szapudi *et al.*, Mon. Not. R. Astron. Soc. **450**, 288 (2015).
[23] P. J. E. Peebles, Astrophys. J. **557**, 495 (2001).
[24] A. V. Tikhonov and A. Klypin, Mon. Not. R. Astron. Soc. **395**, 1915 (2009).
[25] Y. Hoffman and J. Shaham, Astrophys. J. Lett. **262**, L23 (1982).
[26] V. Icke, Mon. Not. R. Astron. Soc. **206**, 1P (1984).

[27] J. A. Fillmore and P. Goldreich, Astrophys. J. **281**, 9 (1984).
[28] E. Bertschinger, Astrophys. J. Suppl. Ser. **58**, 1 (1985).
[29] G. R. Blumenthal, L. N. da Costa, D. S. Goldwirth, M. Lecar, and T. Piran, Astrophys. J. **388**, 234 (1992).
[30] R. K. Sheth and R. van de Weygaert, Mon. Not. R. Astron. Soc. **350**, 517 (2004).
[31] E. Jennings, Y. Li, and W. Hu, Mon. Not. R. Astron. Soc. **434**, 2167 (2013).
[32] A. Friedmann, Z. Phys. **10**, 377 (1922).
[33] G. Lemaître, Ann. Soc. Sci. Bruxelles A **47**, 49 (1927).
[34] H. P. Robertson, Astrophys. J. **82**, 284 (1935).
[35] A. G. Walker, Proc. London Math. Soc. **42**, 90 (1937).
[36] J. M. Bardeen, Phys. Rev. D **22**, 1882 (1980).
[37] H. Kodama and M. Sasaki, Prog. Theor. Phys. Suppl. **78**, 1 (1984).
[38] V. F. Mukhanov, H. A. Feldman, and R. H. Brandenberger, Phys. Rep. **215**, 203 (1992).
[39] C.-P. Ma and E. Bertschinger, Astrophys. J. **455**, 7 (1995).
[40] F. Bernardeau, S. Colombi, E. Gaztañaga, and R. Scoccimarro, Phys. Rep. **367**, 1 (2002).
[41] G. Lemaître, Ann. Soc. Sci. Bruxelles A **53**, 51 (1933).
[42] R. C. Tolman, Proc. Natl. Acad. Sci. U.S.A. **20**, 169 (1934).
[43] H. Bondi, Mon. Not. R. Astron. Soc. **107**, 410 (1947).
[44] P. Szekeres, Commun. Math. Phys. **41**, 55 (1975).
[45] H. Stephani, Commun. Math. Phys. **4**, 137 (1967).
[46] A. Krasiński, *Inhomogeneous Cosmological Models* (Cambridge University Press, Cambridge, England, 1997).
[47] K. Bolejko, A. Krasiński, C. Hellaby, and M.-N. Célérier, *Structures in the Universe by Exact Methods* (Cambridge University Press, Cambridge, England, 2009).
[48] K. Enqvist, Gen. Relativ. Gravit. **40**, 451 (2008).
[49] C. Clarkson, G. Ellis, J. Larena, and O. Umeh, Rep. Prog. Phys. **74**, 112901 (2011).
[50] T. Buchert, Gen. Relativ. Gravit. **32**, 105 (2000).
[51] E. W. Kolb, S. Matarrese, and A. Riotto, New J. Phys. **8**, 322 (2006).
[52] J. Ehlers, Abh. Akad. Wiss. Lit. Mainz, Math.-Naturwiss. Kl. **11**, 793 (1961); English translation: Gen. Relativ. Gravit. **25**, 1225 (1993).
[53] G. F. R. Ellis, in *General Relativity and Cosmology*, Proceedings of the International School of Physics "Enrico Fermi," Course XLVII, edited by R. K. Sachs (Academic Press, New York, 1971), p. 104; reprinted in Gen. Relativ. Gravit. **41**, 581 (2009).
[54] G. F. R. Ellis and H. van Elst, in *Theoretical and Observational Cosmology*, edited by M. Lachièze-Rey, NATO Science Series C Vol. 541 (Kluwer, Dordrecht, 1999), p. 1, arXiv:gr-qc/9812046.
[55] G. F. R. Ellis, R. Maartens, and M. A. H. MacCallum, *Relativistic Cosmology* (Cambridge University Press, Cambridge, England, 2012).
[56] C. B. Collins and J. Wainwright, Phys. Rev. D **27**, 1209 (1983).
[57] S. W. Hawking and G. F. R. Ellis, *The Large Scale Structure of Space-Time* (Cambridge University Press, Cambridge, England, 1973).
[58] M. Bartelmann and P. Schneider, Phys. Rep. **340**, 291 (2001).
[59] R. K. Sachs, Proc. R. Soc. A **264**, 309 (1961).
[60] I. M. H. Etherington, Philos. Mag. **15**, 761 (1933).
[61] G. F. R. Ellis, S. D. Nel, R. Maartens, W. R. Stoeger, and A. P. Whitman, Phys. Rep. **124**, 315 (1985).
[62] L. Amendola, M. Kunz, and D. Sapone, J. Cosmol. Astropart. Phys. 04 (2008) 013.
[63] P. Zhang, M. Liguori, R. Bean, and S. Dodelson, Phys. Rev. Lett. **99**, 141302 (2007).
[64] R. Reyes, R. Mandelbaum, U. Seljak, T. Baldauf, J. E. Gunn, L. Lombriser, and R. E. Smith, Nature (London) **464**, 256 (2010).
[65] A. Lichnerowicz, J. Math. Pures Appl. **23**, 37 (1944).
[66] J. W. York, Jr., Phys. Rev. Lett. **28**, 1082 (1972).
[67] P. Melchior, P. M. Sutter, E. S. Sheldon, E. Krause, and B. D. Wandelt, Mon. Not. R. Astron. Soc. **440**, 2922 (2014).
[68] J. Clampitt and B. Jain, Mon. Not. R. Astron. Soc. **454**, 3357 (2015).
[69] D. J. Eisenstein and W. Hu, Astrophys. J. **496**, 605 (1998).
[70] Planck Collaboration, N. Aghanim *et al.*, Astron. Astrophys. **641**, A6 (2020).
[71] P. Coles and B. Jones, Mon. Not. R. Astron. Soc. **248**, 1 (1991).
[72] S. D. Landy and A. S. Szalay, Astrophys. J. **412**, 64 (1993).
[73] S. D. M. White, Mon. Not. R. Astron. Soc. **186**, 145 (1979).
[74] P. J. E. Peebles, *The Large-Scale Structure of the Universe* (Princeton University Press, Princeton, NJ, 1980).
[75] J. R. Gott III, A. L. Melott, and M. Dickinson, Astrophys. J. **306**, 341 (1986).
[76] A. J. S. Hamilton, J. R. Gott III, and D. Weinberg, Astrophys. J. **309**, 1 (1986).
[77] K. R. Mecke, T. Buchert, and H. Wagner, Astron. Astrophys. **288**, 697 (1994).
[78] N. D. Padilla, L. Ceccarelli, and D. G. Lambas, Mon. Not. R. Astron. Soc. **363**, 977 (2005).
[79] S. Alam *et al.* (BOSS Collaboration), Mon. Not. R. Astron. Soc. **470**, 2617 (2017).
[80] S. Alam *et al.* (eBOSS Collaboration), Phys. Rev. D **103**, 083533 (2021).
[81] B. R. Granett, M. C. Neyrinck, and I. Szapudi, Astrophys. J. Lett. **683**, L99 (2008).
[82] G. C. McVittie, Mon. Not. R. Astron. Soc. **93**, 325 (1933).
[83] A. J. S. Hamilton, Astrophys. J. Lett. **385**, L5 (1992).
[84] N. Kaiser, Mon. Not. R. Astron. Soc. **227**, 1 (1987).
[85] Y.-C. Cai, A. Taylor, J. A. Peacock, and N. Padilla, Mon. Not. R. Astron. Soc. **462**, 2465 (2016).
[86] S. Nadathur and W. J. Percival, Mon. Not. R. Astron. Soc. **483**, 3472 (2019).
[87] F. Beutler *et al.*, Mon. Not. R. Astron. Soc. **423**, 3430 (2012).
[88] C. Howlett, A. J. Ross, L. Samushia, W. J. Percival, and M. Manera, Mon. Not. R. Astron. Soc. **449**, 848 (2015).
[89] C. Blake *et al.*, Mon. Not. R. Astron. Soc. **456**, 2806 (2016).
[90] A. R. Pullen, S. Alam, S. He, and S. Ho, Mon. Not. R. Astron. Soc. **460**, 4098 (2016).
[91] S. Alam, H. Miyatake, S. More, S. Ho, and R. Mandelbaum, Mon. Not. R. Astron. Soc. **465**, 4853 (2017).
[92] E. V. Linder, Phys. Rev. D **72**, 043529 (2005).
[93] H. Akaike, IEEE Trans. Autom. Control **19**, 716 (1974).
[94] J. M. Bardeen, J. R. Bond, N. Kaiser, and A. S. Szalay, Astrophys. J. **304**, 15 (1986).

[95] A. Banerjee and T. Abel, Mon. Not. R. Astron. Soc. **500**, 5479 (2021).
[96] E. Gaztañaga, Mon. Not. R. Astron. Soc. **268**, 913 (1994).
[97] D. J. Croton *et al.*, Mon. Not. R. Astron. Soc. **352**, 1232 (2004).
[98] E. Platen, R. van de Weygaert, and B. J. T. Jones, Mon. Not. R. Astron. Soc. **380**, 551 (2007).